© 2014. Published by The Company of Biologists Ltd | Journal of Cell Science (2014) 127, 4620–4633 doi:10.1242/jcs.150474

RESEARCH ARTICLE

Positive feedback between Golgi membranes, microtubules and ER exit sites directs *de novo* biogenesis of the Golgi

Paolo Ronchi[1], Christian Tischer[2], Devrim Acehan[3] and Rainer Pepperkok[1,2,*]

ABSTRACT

The Golgi complex is the central organelle of the secretory pathway. It undergoes dynamic changes during the cell cycle, but how it acquires and maintains its complex structure is unclear. To address this question, we have used laser nanosurgery to deplete BSC1 cells of the Golgi complex and have monitored its biogenesis by quantitative time-lapse microscopy and correlative electron microscopy. After Golgi depletion, endoplasmic reticulum (ER) export is inhibited and the number of ER exit sites (ERES) is reduced and does not increase for several hours. Occasional fusion of small post-ER carriers to form the first larger structures triggers a rapid and drastic growth of Golgi precursors, due to the capacity of these structures to attract more carriers by microtubule nucleation and to stimulate ERES biogenesis. Increasing the chances of post-ER carrier fusion close to ERES by depolymerizing microtubules results in the acceleration of Golgi and ERES biogenesis. Taken together, on the basis of our results, we propose a self-organizing principle of the early secretory pathway that integrates Golgi biogenesis, ERES biogenesis and the organization of the microtubule network by positive-feedback loops.

KEY WORDS: ER exit site biogenesis, Golgi biogenesis, Early secretory pathway organization, Laser nanosurgery

INTRODUCTION

How organelles are formed and what determines their shape, size and intracellular position are fundamental questions in cell biology. Two alternative mechanisms can play a role in the biogenesis of a cellular organelle. The first one is to copy a template acquired early during evolution. This model is generally accepted for the endoplasmic reticulum (ER) and mitochondria, which act as templates for their own biogenesis and growth before their mitotic partitioning in daughter cells (Palade, 1983; Warren and Wickner, 1996). The second mechanism is self-organization, which is a well-established paradigm in cell biology from the molecular to the organismal level (Gerstman and Chapagain, 2005; Misteli, 2001; Wennekamp et al., 2013). Self-organization is defined as the capacity of an organelle to acquire its own shape *de novo* as a result of the interaction of its components. At the subcellular level, this model has been suggested to apply, for instance, to the organization and architecture of the cytoskeleton (Nédélec et al., 1997; Vignaud et al., 2012).

How the Golgi complex acquires and maintains its structure is not completely clear. This organelle is evolutionarily conserved in all eukaryotic cells (Dacks et al., 2009). Although its structure has varied significantly during evolution, its basic molecular composition has been very well conserved, together with its fundamental role in the secretory pathway. In most eukaryotic organisms, the Golgi complex is composed of stacked flattened cisternae, and in mammalian cells it has an additional complexity level due to the lateral linking of its stacked units in the perinuclear area to form a ribbon (Wei and Seemann, 2010). Despite its complex organization, the Golgi complex is a very dynamic organelle (Lippincott-Schwartz and Zaal, 2000), and it undergoes dramatic structural changes during mitosis (Wei and Seemann, 2009). During interphase, it receives material from the ER and the endosomal system and gives rise to several anterograde and retrograde transport pathways. Nonetheless, an overall stable structure is correctly generated as a result of these highly dynamic events. Moreover, the morphology and size of the Golgi complex depend on the balanced flux of membranes that pass through it (Glick, 2000; Trucco et al., 2004; Guo and Linstedt, 2006; Griffiths et al., 1989), and the input of material from the ER is crucial for its homeostasis (Zaal et al., 1999; Storrie et al., 1998). These observations make the Golgi complex a good candidate for a case of a self-organizing organelle. The self-organization model postulates that the Golgi complex should be able to form *de novo* as a result of the fusion of membranes derived from the ER, and many independent studies suggest that this could be the case (Lippincott-Schwartz et al., 1989; Miles et al., 2001; Ward et al., 2001; Puri and Linstedt, 2003; Kasap et al., 2004; Altan-Bonnet et al., 2006; Tängemo et al., 2011). Nonetheless, other studies have reported the possibility of a template-mediated Golgi assembly, implicating the Golgi matrix proteins in functioning as seeds or templates for biogenesis (Jesch et al., 2001; Shorter and Warren, 2002; Seemann et al., 2002; Axelsson and Warren, 2004). To what extent Golgi biogenesis can be considered a self-assembly process is therefore still not clear (Lowe and Barr, 2007; Wang and Seemann, 2011).

The ER exit sites (ERES) are the sites of production of post-ER carriers directed to the Golgi complex – ribosome-free ER subdomains that produce coat protein complex II (COPII)-coated transport vesicles. In cultured mammalian cells, ERES are distributed throughout the entire cytoplasm, with an accumulation in the juxta-nuclear area close to the Golgi complex (Hammond and Glick, 2000; Budnik and Stephens, 2009). During mitosis, coincident with the Golgi breakdown, the recruitment of COPII components is dramatically reduced and ER export is blocked (Prescott et al., 2001; Kano et al., 2004). Upon mitotic exit, when reassembly of the Golgi complex requires the restoration of an efficient ER export process, COPII proteins are again efficiently

[1]European Molecular Biology Laboratory (EMBL), Cell biology and biophysics unit. [2]European Molecular Biology Laboratory (EMBL), Advanced Light Microscopy. [3]European Molecular Biology Laboratory (EMBL), Electron Microscopy Core Facilities, Meyerhofstrasse 1, 69117 Heidelberg, Germany.

*Author for correspondence (pepperko@embl.de)

Received 24 January 2014; Accepted 18 August 2014

Journal of Cell Science

Journal of Cell Science (2014) 127, 4620–4633 doi:10.1242/jcs.150474

recruited to the ER membrane (Hammond and Glick, 2000; Altan-Bonnet et al., 2006; Budnik and Stephens, 2009). How they achieve their interphase distribution with an accumulation in proximity to the juxta-nuclear Golgi complex is not clear. It has been proposed that ERES distribution depends on the scaffolding function of Sec16, a peripheral membrane protein (Connerly et al., 2005; Ivan et al., 2008; Hughes et al., 2009). This view has been recently challenged, and a self-organizing process underlying the early secretory pathway has been suggested, with a putative role of Golgi-localized tethers in the localization of ERES (Glick, 2014).

Although the secretory pathway has been largely explored in the last decades and our knowledge of the molecular details is continuously progressing, how dynamic processes such as ER export, Golgi formation and microtubule network organization are integrated to give rise to and maintain the organization of this membrane system is not clear. To address this question, we made use of a recently developed technique to deplete the Golgi complex from living cells by laser nanosurgery and monitor its subsequent biogenesis (Tängemo et al., 2011; Ronchi et al., 2012; Ronchi and Pepperkok, 2013). This approach has provided direct evidence

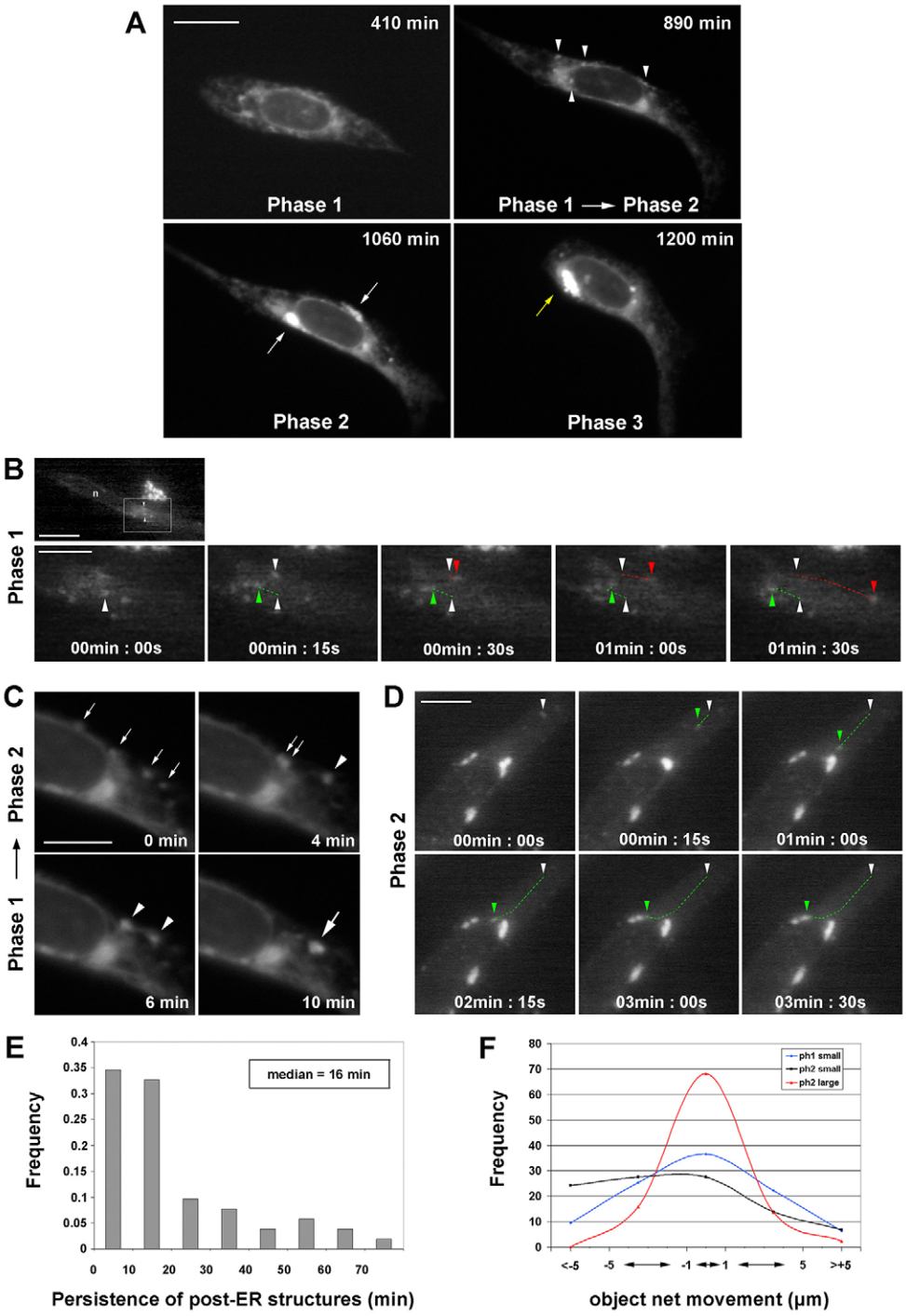

Fig. 1. See next page for legend.

Journal of Cell Science (2014) 127, 4620–4633 doi:10.1242/jcs.150474

Fig. 1. Time-lapse characterization of *de novo* Golgi biogenesis. Ten YT2 cells were dissected by laser nanosurgery in order to completely remove the Golgi complex. Golgi biogenesis was subsequently followed by time-lapse microscopy. (A) Example of Golgi biogenesis in a YT2 cell followed at 2-min intervals (supplementary material Movie 1). Four characteristic time-points of the time-lapse are shown. Phase 1 shows a steady-state accumulation of the Golgi marker in the ER. At the transition between phase 1 and 2, post-ER structures were visible over the ER background (arrowheads). During phase 2, larger and brighter Golgi precursors could be identified (white arrows). Finally, in phase 3, all post-ER material clustered at a single perinuclear position (yellow arrow). Scale bar: 20 μm. (B) A YT2-expressing karyoplast was followed by time-lapse imaging with low time resolution (30-min intervals) until several small phase 1 carriers could be identified (top panel). Then, images were taken every 15 s to track the movement of the small carriers. In the lower panels, the boxed area is magnified and two carriers moving in opposite directions are shown. White arrowheads indicate their position at the beginning of the acquisition and the dashed lines highlight their trajectories (green, moving towards the nucleus; red, moving towards the periphery). n, nucleus. Scale bars: 20 μm (upper panel), 10 μm (lower panel). (C) Subsequent frames of the time-lapse experiment described in A. At the transition between phase 1 and 2 (~900 min after nanosurgery) post-ER carriers fused with one another. Four small structures (0 min, small arrows) fused to form two intermediate ones (4 and 6 min, arrowheads), which finally fused into a single large object (10 min, large arrow). Scale bar: 10 μm. (D) YT2-expressing karyoplasts were imaged by time-lapse microscopy with lower time resolution until they reached phase 2. Then, imaging was performed as described for B. The gallery shows a small carrier moving from the cell periphery to the perinuclear area to fuse with a larger Golgi intermediate. Scale bar: 10 μm. (E) YT2 karyoplasts were imaged as described for A. A total of 103 post-ER structures identified in three different phase 1 cells were followed over time. The lifetime was measured and the distribution of their persistence is plotted. (F) Karyoplasts in phases 1 and 2 were imaged as described for B and D, and the movements of post-ER structures were tracked. A total of 63 tracks recorded in eight different cells were analyzed for small carriers in phase 1 (blue curve); 30 and 43 tracks recorded from five cells were analyzed for small (black curve) and large (red curve) structures, respectively, in phase 2. Over a 5-min acquisition period, their net movements were determined with respect to the reference point chosen in the centre of the nucleus. The objects were divided into five classes according to their movement distances, and the frequency of distribution is plotted. Negative values represent movements towards the reference point and positive values show movement towards the periphery.

for Golgi *de novo* biogenesis in mammalian cells (Tängemo et al., 2011). Here, we have further characterized this process by using quantitative time-lapse imaging correlated with electron microscopy. Our data demonstrate that the mechanisms underlying Golgi *de novo* biogenesis and the organization of the early secretory pathway are governed by self-organizing principles.

RESULTS

Quantitative time-lapse imaging reveals three phases of Golgi *de novo* biogenesis

The Golgi complex can be *de novo* synthesized after its depletion from BSC1 cells (a renal epithelial cell line of African green monkey origin) by laser nanosurgery (Tängemo et al., 2011). To gain a better insight into this process, we quantitatively analyzed the dynamics of the YFP-tagged Golgi enzyme GalNAc-T2–YFP (YT2; Axelsson and Warren, 2004) in karyoplasts with high temporal resolution time-lapse microscopy and correlative light and electron microscopy. Based on time-lapse analysis of at least ten cells, three distinct phases of Golgi biogenesis could be observed (Fig. 1A; supplementary material Movie 1). In phase 1, the karyoplasts synthesized the YFP-tagged Golgi marker, which increased in intensity in the ER over time (Fig. 2A), and small post-ER carriers were occasionally produced (Fig. 1A,B; Fig. 2A). These carriers moved on linear tracks, consistent with microtubule-mediated transport, but without any preferential directionality (Fig. 1B,F). These structures were not substantially accumulated over time in the cell, and they disappeared on average 16 min after their formation (Fig. 1E), most likely owing to their reabsorption into the ER and/or degradation. Quantification showed that, despite the increase in the total amount of YFP-tagged Golgi marker synthesized after laser nanosurgery, the total fluorescence of the observed small post-ER carriers remained very low in phase 1 compared with the subsequent phases (Fig. 2A; supplementary material Fig. S1A). In order to compare the time-lapse analysis curves of the karyoplasts, we calculated the parameter Δt (Fig. 2A,C), which represents a measure of the difference between the start of protein synthesis and net ER export. This parameter displayed a median delay for secretion of 354 min, demonstrating that post-ER material accumulation is inhibited after Golgi removal in most cells. As a result of this low efficiency of net ER export, YT2 accumulated in the ER (Fig. 1A; Fig. 2E). By contrast, when the Golgi complex was only partially depleted by laser nanosurgery the total fluorescence of post-ER structures increased with the same kinetics as the total amount of the marker-specific cellular fluorescence (Fig. 2B), and the median Δt was only 6 min. No accumulation of the fluorescent marker in the ER was observed under these conditions (Fig. 2E). The observed inhibition of ER exit during phase 1 did not appear to be specific for the Golgi marker YT2, as the cargo protein GPI–CFP (Keller et al., 2001) displayed the same behavior after laser nanosurgery (supplementary material Fig. S1B). However, this ER export inhibition does not represent a general inhibition of intracellular trafficking as the internalization of transferrin and EGF occurred with no changes compared with that observed in unperturbed control cells (supplementary material Fig. S2A,B).

At the transition from phase 1 to phase 2 (656±173 min after nanosurgery; ±s.d.) the small post-ER carriers occasionally collided and fused with each other. This resulted in the formation of more stable and larger structures (Fig. 1C). After their formation, these structures grew further in size and became predominantly located in the juxta-nuclear area during phase 2. Interestingly, they were able to frequently attract and absorb smaller carriers even from the cell periphery (Fig. 1D). In contrast to the small post-ER carriers observed in phase 1, phase 2 small carriers showed directional movements from the cell periphery towards the cell nucleus (Fig. 1D,F). Quantification showed that the total fluorescence of post-ER structures rapidly increased within 171±88 min in phase 2, from 20% to 60% of the maximum intensity reached during the experiment (Fig. 2A; supplementary material Fig. S1A). The onset of this burst of Golgi precursor synthesis was not dependent on the amount of fluorescent Golgi marker expressed (supplementary material Fig. S1B). To compare the kinetics of post-ER material accumulation during phase 2 in the ten karyoplasts analysed, we measured the average slope of the secretion curves in phase 2 and normalized for the slope of the protein synthesis curve in the same interval (Fig. 2D). In cells where the Golgi was not entirely removed the median ratio was 1.05, whereas after complete Golgi removal the cells displayed a median ratio value of 1.95, indicating that, in the latter case, the kinetics of net ER export in phase 2 were faster than the synthesis.

Finally, in phase 3 the larger structures that formed during phase 2 clustered in a single juxta-nuclear location (Fig. 1A). Interestingly, the position of the new Golgi complex in phase 3 did not appear to be biased towards one side of the nucleus

Journal of Cell Science (2014) 127, 4620–4633 doi:10.1242/jcs.150474

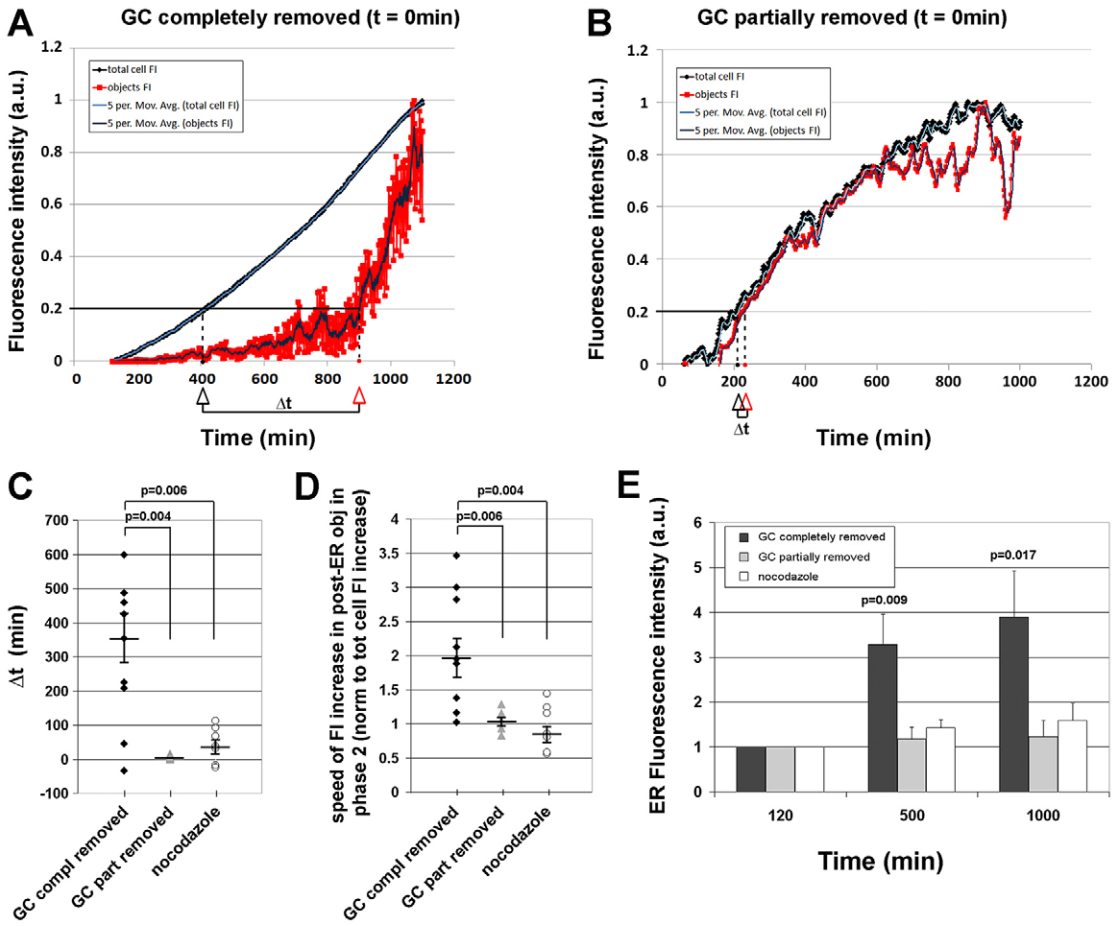

Fig. 2. Bimodal kinetics of the accumulation of post-ER material during Golgi biogenesis. (A) YT2 cells were treated as for Fig. 1A and analyzed by Morphoquant to segment post-ER structures. The plot shows the changes of the total cellular fluorescence intensity (FI) of the Golgi complex (GC) marker YT2 (black line) and the fluorescence intensity in segmented structures (red line) over time. Both fluorescence intensity values have been rescaled from 0 (lowest value of the time-lapse) to 100 (maximum value) for easier comparison of the kinetics of material accumulation in the Golgi precursors (objects) with total protein levels. The time-points at which 20% of the maximum fluorescence intensity was reached by each curve are highlighted and their difference Δt is represented. a.u., arbitrary units. (B) YT2 cells were dissected by laser nanosurgery, intentionally leaving part of the Golgi complex in the karyoplast. Time-lapse experiments were analyzed and results were plotted as described for A. (C) From several curve profiles determined as described for A and B, the delay Δt for karyoplasts where the Golgi complex was completely or partially removed was measured. Δt values of single cells are plotted, and the horizontal line represents the median value (±s.e.m.). The same analysis was conducted on nocodazole-treated karyoplasts (Fig. 8) and the results are plotted. (D) The same curve profiles used for the analysis in C were analyzed as follows: the average slope of the fluorescence intensity curve of the objects was calculated in the interval between 20% and 60% of its maximum value. This value was then normalized for the slope of the total cell fluorescence intensity curve in the same interval, and the results for individual cells are plotted together with the median value of the distribution (±s.e.m.). (E) Cells were dissected, treated as indicated and imaged by time-lapse microscopy. The fluorescence intensity of the ER was measured as the integrated density of YT2 signal in areas devoid of post-ER structures (normalized for the considered area) at the beginning of the acquisition (120 min after nanosurgery), at 500 min and at 1000 min. The results were divided by the values of the first time-point to determine the changes in YT2 ER levels during Golgi biogenesis. Data show the mean+s.e.m. Statistical significance in C,D and E was assessed by using Student's *t*-test.

(supplementary material Fig. S1D), suggesting that there is no memory of where the organelle had been located prior to the nanosurgery.

Ultrastructural and molecular characterization of Golgi precursors during *de novo* biogenesis

In order to gain ultrastructural details of Golgi precursors during the biogenesis process, we used correlative light and electron microscopy (CLEM; supplementary material Fig. S3). In agreement with our previously published results (Tängemo et al., 2011), phase 1 karyoplasts showed no evidence of stacked Golgi-like structures (Fig. 3). By contrast, we could identify ERES, which appeared to be structurally normal (Fig. 3A), and occasionally we observed electron-dense accumulations in the ER lumen (Fig. 3B). At the transition between phase 1 and 2 electron microscopy analysis showed small clusters of vesicles and tubules (Fig. 3C).

Interestingly, analysis of phase 2 cells by CLEM revealed that the larger structures forming during this phase were generally not showing a typical Golgi-like ultrastructure (Fig. 3D). They represented clusters of juxtaposed membrane-bounded structures, which appeared to be compact and convoluted (Fig. 3D–F). Some structures in the cluster started to flatten and acquired cisternae-like shapes (Fig. 3E). The regular spacing and the presence of electron-dense material in the lumen of these flattened areas was indicative of the presence of a molecular bridge between the two membranes (Fig. 3E,F). Furthermore, the close association and the constant spacing between the peripheral membranes of adjacent structures

Journal of Cell Science (2014) 127, 4620–4633 doi:10.1242/jcs.150474

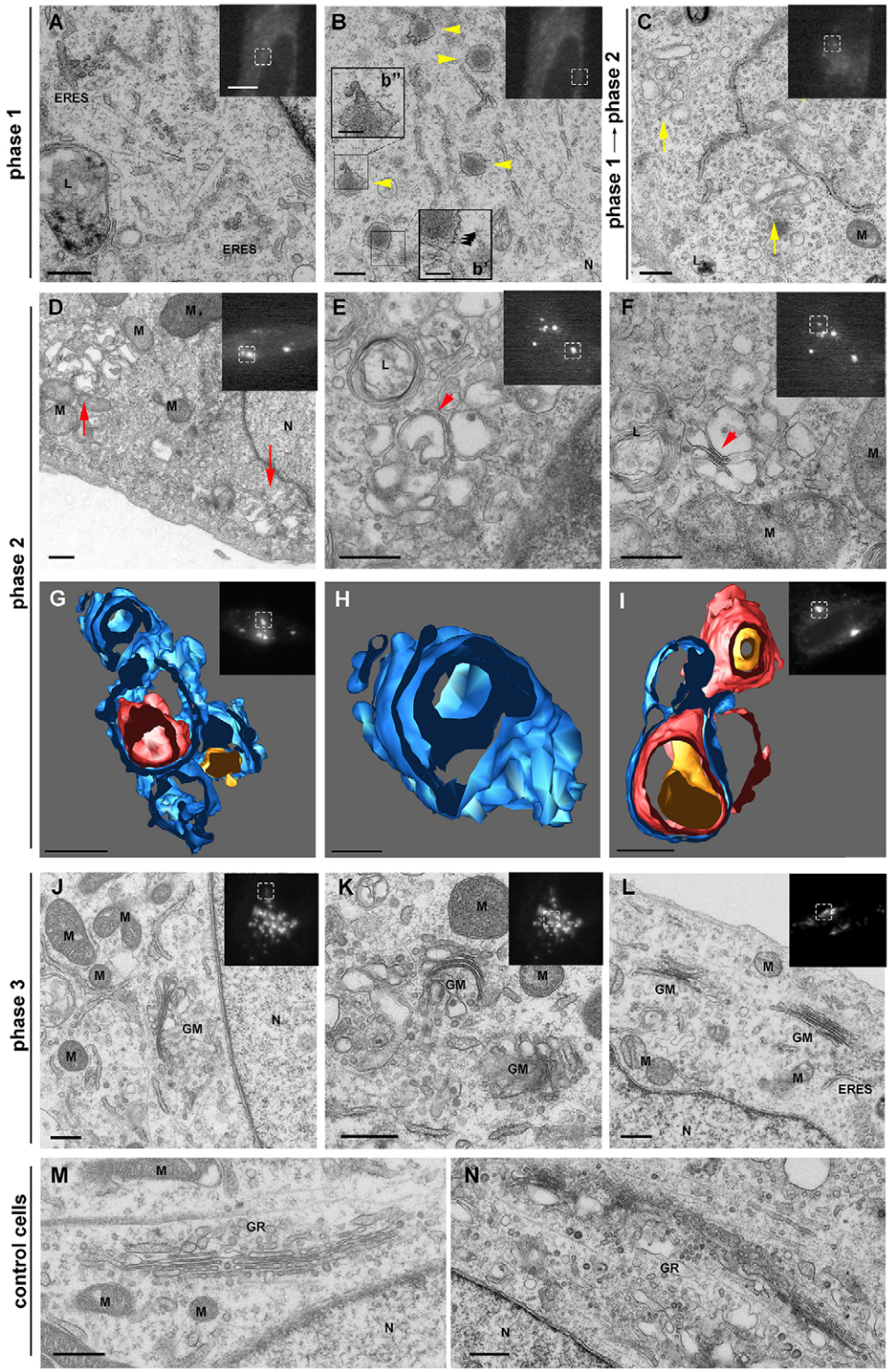

Fig. 3. Ultrastructural characterization of Golgi biogenesis. YT2 cells were dissected by laser nanosurgery and followed by time-lapse microscopy until they reached the phase of interest. Cells were then fixed and processed for correlative light and electron microscopy. Fluorescence images of the karyoplasts before fixation are shown in the insets, where the area represented in the electron microscopy image is boxed. (A,B) Phase 1 cells do not show any Golgi-like structures, but other organelles (e.g. ERES) could be identified and have a normal morphology (A). Other karyoplasts present electron-dense accumulations (yellow arrowheads in B) in the ER lumen (the ER identity of these membranes is demonstrated by the association of ribosomes – arrowheads in the inset b′), often in proximity to ERES (enlarged in b″). (C) Tubular-vesicular clusters of membranes could be occasionally identified in karyoplasts at the transition between phase 1 and 2 (yellow arrows). (D–F) Phase 2 cells show larger clusters of convoluted membranes (red arrows in D), with flattened profiles consistent with cisternal precursors (red arrowheads). (G–I) Electron microscopy tomography reconstruction of YT2-positive structures in two different karyoplasts in phase 2. The same color indicates that membranes are in continuity. (H) An area of the structure in G at higher magnification to highlight the two layers of cisternae emerging from the same vesicle. (I) An example of a more advanced stage of phase 2 Golgi biogenesis, where two cisternae are stacked. (J–L) Examples of Golgi ministacks in karyoplasts in phase 3. (M,N) Control cells neighboring the karyoplasts present complete Golgi ribbons. N, nucleus; M, mitochondrion; L, lysosome; GM, Golgi ministack; GR, Golgi ribbon. Scale bars: 10 µm (light microscopy images), 500 nm (conventional electron microscopy micrographs), 200 nm (b′,b″) 300 nm (G,I), 100 nm (H).

suggested the initiation of lateral stacking (Fig. 3E,F). To gain better insight into the ultrastructure of Golgi precursors during phase 2 of Golgi biogenesis, we used electron tomography. Three-dimensional (3D) reconstruction showed a convoluted network of membranes forming interconnected structures (Fig. 3G–I; supplementary material Movie 2). Most of these structures had cavities and cisterna-like features. The precursors did not show any connection with the neighboring ER, confirming their post-ER nature. Only occasionally (1/9) did phase 2 karyoplasts show ministack-like structures, suggesting that this is the crucial phase for the maturation of the Golgi into a stacked structure. Accordingly, phase 3 cells presented clusters of Golgi ministacks (Fig. 3J–L). Nonetheless, in contrast to the Golgi complex of control cells (Fig. 3M,N), phase 3 structures did not form complete Golgi ribbons within 24 h after nanosurgery. Taken together, these electron microscopy analyses suggest that the building of a stacked Golgi occurs by remodeling of the precursor interconnected membrane structures observed during phase 2.

Journal of Cell Science (2014) 127, 4620–4633 doi:10.1242/jcs.150474

Next, we set out to characterize the molecular composition of the Golgi precursors. We have previously shown that our nanosurgery procedure strongly depletes many Golgi-associated proteins (Tängemo et al., 2011). We performed immunolabeling experiments with karyoplasts fixed in the different phases of biogenesis in order to monitor the presence of the Golgi proteins GM130, GRASP55, GRASP65, giantin, AKAP450 and CLASP2 (Fig. 4). As expected, in phase 1, very low levels of all the tested proteins were present. Interestingly, in phase 2, the levels of GM130, GRASPs and CLASP2 in Golgi precursors increased to ~10–15% of their amount in neighboring control cells, whereas the amount of giantin and AKAP450 remained low, suggesting that different proteins associate with Golgi precursors at different time-points and might contribute to different biogenesis steps. In phase 3 cells, Golgi elements contained 16–30% of control cell levels, proving that this amount is sufficient to build stacked structures.

ERES biogenesis and subcellular distribution correlate with those of the Golgi

Next, we set out to obtain possible explanations for the bimodal kinetics of ER export during phases 1 and 2 of Golgi biogenesis. To this end, we analyzed ERES in karyoplasts in the different phases of the process and quantified their features. Immunofluorescence experiments revealed that ERES were present throughout all phases of Golgi *de novo* biogenesis and the amounts of the COPII component Sec31A per cell area remained largely unchanged throughout all phases (Fig. 5A,B). By contrast, the number of ERES in early and late phase 1 cells was drastically reduced to 22±5% and 18±4% (±s.e.m.,) of the number observed in control cells, respectively (Fig. 5C). Although these data seem to be contradictory, they could be explained by the existence of a large non-membrane-associated fraction of the protein at steady state, consistent with previously reported data (Koreishi et al., 2013). The reduction in the number

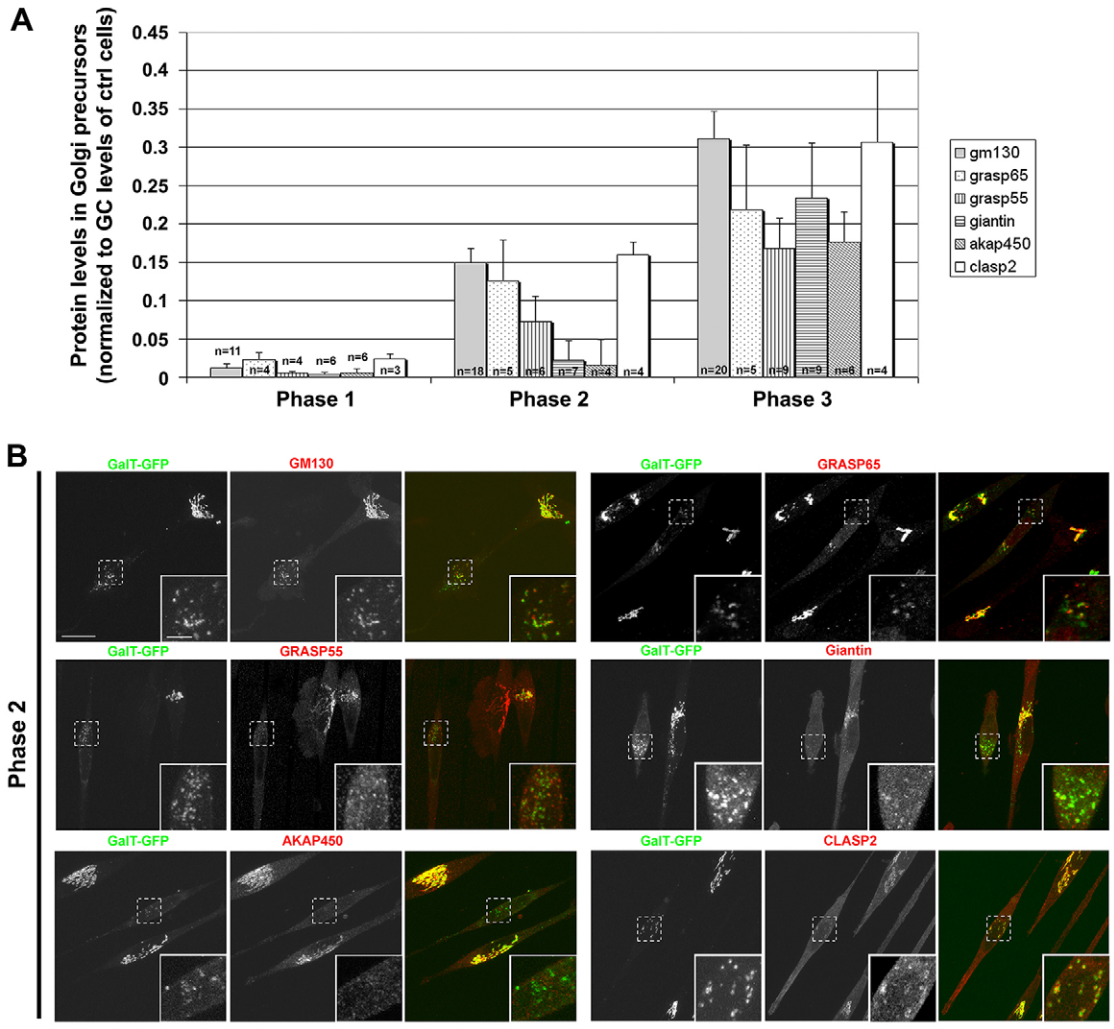

Fig. 4. Molecular composition of Golgi precursors in the different phases of *de novo* biogenesis. Karyoplasts in different phases of Golgi biogenesis were fixed and immunostained for different Golgi complex (GC) markers. (A) Post-ER objects were segmented and the amount of each marker was measured. The values for the karyoplasts were then divided by the average amount of the same marker in the Golgi of control cells in the same image. The histogram represents the median (+s.e.m.) value of different karyoplasts in each phase (*n* is represented on each column). Ctrl, control. (B) Examples of immunolabeling of phase 2 karyoplasts with six different Golgi markers. The GalT–GFP image is considered as the reference to determine the phase of Golgi biogenesis. The area enclosed by the dashed line is shown at higher magnification in the inset. Scale bars: 20 µm (main image), 5 µm (inset).

Journal of Cell Science (2014) 127, 4620–4633 doi:10.1242/jcs.150474

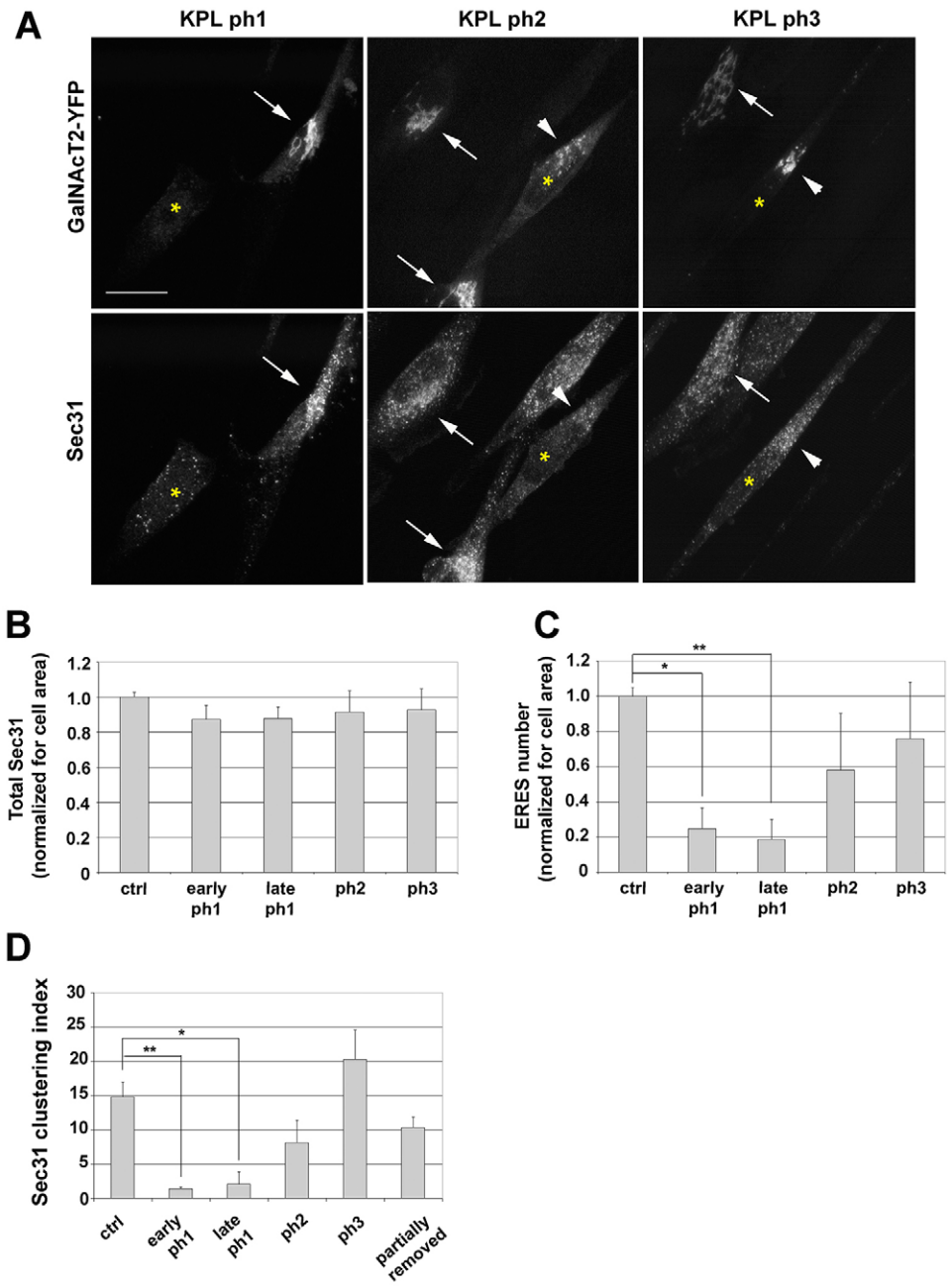

Fig. 5. ERES number and spatial distribution during Golgi biogenesis. (A) Karyoplasts (KPL) were fixed with paraformaldehyde during different phases of Golgi biogenesis and were immunostained for Sec31A. Confocal *Z*-stacks of images covering the entire cell were acquired and the sum intensity projection is shown. Arrows indicate the Golgi area in control cells; arrowheads indicate areas where the precursors accumulate in the karyoplast; the yellow asterisks indicate the karyoplasts. Scale bar: 10 μm. (B) After background subtraction, cells were manually segmented. The total Sec31 fluorescence intensity was measured and divided by the cell area. The fluorescence intensity levels of the karyoplasts were normalized to the average of control (ctrl) non-cut cells in the same image. The histogram shows the median (+s.e.m.) of the values for each phase. $n=50$ (ctrls), 8 (early ph1), 9 (late ph1), 8 (ph2), 12 (ph3). (C) From the same images used for the quantification shown in B, the number of ERES was estimated as described in Materials and Methods. The data show the median (+s.e.m.) of the values for each phase. $^{*}P=1.09\times10^{-6}$; $^{**}P=9.28\times10^{-8}$. (D) The ERES clustering index of karyoplasts in different phases of Golgi biogenesis, of untreated cells (ctrl) and of cells where the Golgi had been partially removed was determined as described in Materials and Methods. $n=100$ (ctrl), 9 (early ph1), 9 (late ph1), 8 (ph2), 12 (ph3), 11 (partially removed). The data show the median of the values for each phase (+s.e.m.); $^{*}P=0.014$; $^{**}P=0.0065$.

of ERES could provide a plausible explanation for the ER exit inhibition we observed during phase 1 of Golgi *de novo* biogenesis. Consistent with this, during phase 2 and phase 3, when ER exit was apparently restored, the number of ERES increased again to 63±34% and 94±40% of the number observed in control cells, respectively (Fig. 5C).

Not only was the number of ERES altered during the phases of Golgi *de novo* biogenesis, but their spatial distribution was also affected. In contrast to control cells, where an accumulation of Sec31A-positive ERES in proximity to the Golgi complex could be observed (Fig. 5A,D), in phase 1 cells ERES were distributed throughout the karyoplasts without any apparent accumulation in a juxta-nuclear region (Fig. 5A,D). A similar reduction in polarized distribution was observed for the early endosomal marker EEA1 (supplementary material Fig. S2C,D). A likely explanation for these observations is that ERES and endosomes that initially localize in proximity to the Golgi complex might be depleted together with the Golgi during laser nanosurgery. During phase 2, ERES started to accumulate in proximity to newly forming Golgi precursors and a full restoration of the ERES distribution compared with that of control cells was achieved during phase 3 (Fig. 5A,D), despite the lack of the centrosome (Tängemo et al., 2011). By contrast, a full restoration of the early endosome distribution in proximity to newly forming Golgi membranes could not be observed even for phase 3 cells (supplementary material Fig. S2C,D). We further tested the behavior of Sec16, an ERES component believed to be involved in the early steps of ERES formation (Ivan et al., 2008). Colocalization analysis between Sec16 and Sec31 showed a good overlap of the two proteins during all phases of Golgi biogenesis

Journal of Cell Science (2014) 127, 4620–4633 doi:10.1242/jcs.150474

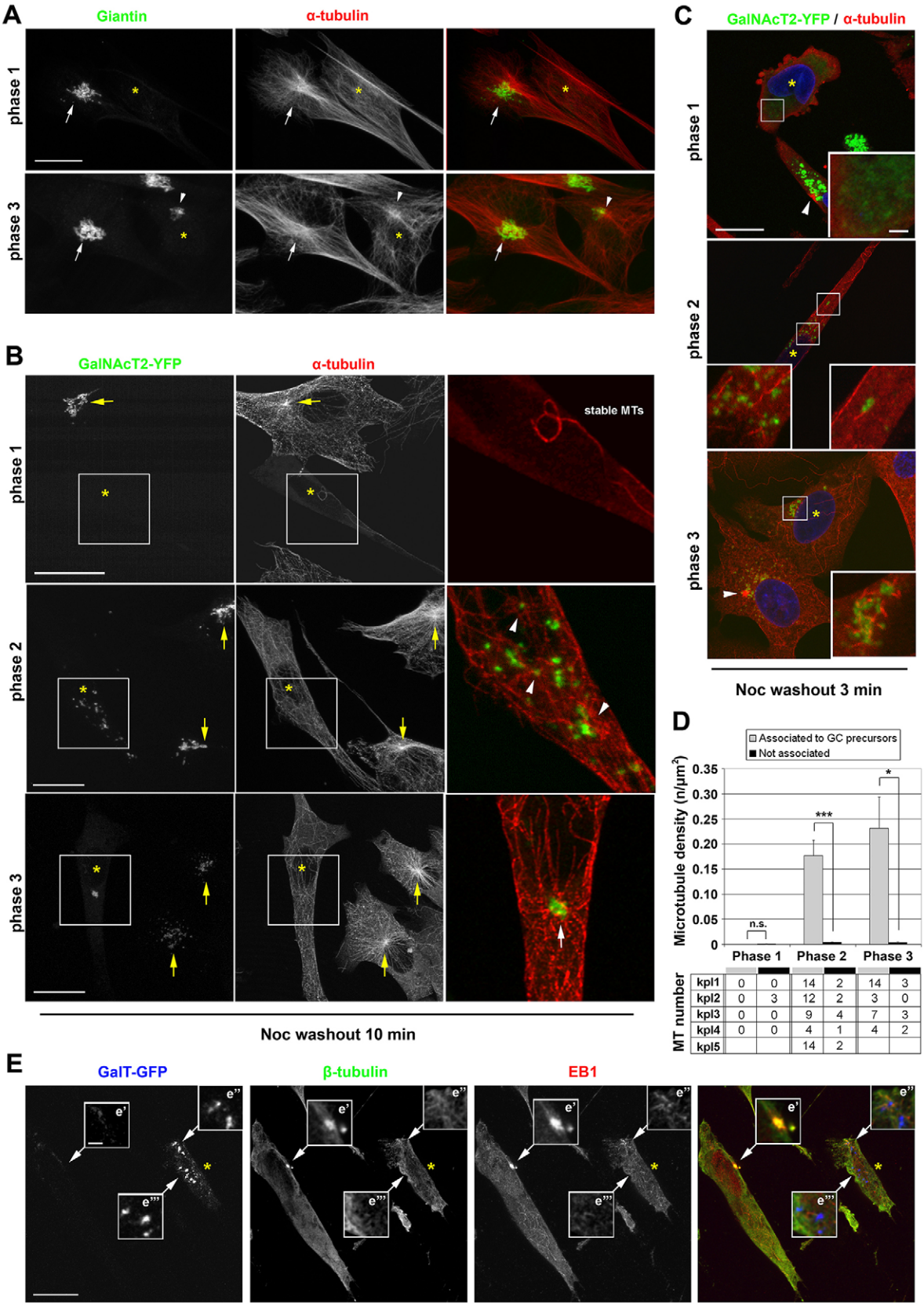

Fig. 6. See next page for legend.

Journal of Cell Science (2014) 127, 4620–4633 doi:10.1242/jcs.150474

Fig. 6. Microtubule network organization during Golgi biogenesis. (A) Karyoplasts in phase 1 (upper panel, asterisk) and in phase 3 (lower panel, asterisk) were fixed and immunostained for the Golgi marker giantin and for α-tubulin. Confocal *Z*-stacks were acquired and their sum projection is shown. The arrows indicate the pericentrosomal microtubule organization in control cells. In the lower panel, the central organization is restored in phase 3 next to the reformed Golgi complex (arrowhead). Scale bar: 20 μm. (B) At different stages of Golgi biogenesis, YT2 cells were treated with 10 μM nocodazole (noc) for 30 min. The drug was then washed out and cells were fixed 10 min thereafter and immunostained for α-tubulin. Separate channels are shown in the first and second columns and the merge of the boxed area is enlarged (3×) in the third column. Asterisks indicate the karyoplasts. Yellow arrows indicate centrosome-nucleated asters of microtubules (MTs) in control cells. White arrowheads and arrows indicate small organized microtubule networks in proximity to Golgi precursors in phase 2 and 3 karyoplasts, respectively. Scale bars: 20 μm. (C) Cells were treated as in B, but were fixed at 3 min after nocodazole washout. The merged image of Hoechst 33342 (blue), YT2 (green) and tubulin (red) is shown. Asterisks indicate the karyoplasts; arrowheads show asters of microtubules nucleated at the centrosome. The insets are enlargements of the boxed areas. Scale bars: 20 μm (main image), 2 μm (inset). (D) The number of microtubules associated or not associated with Golgi complex (GC) precursors was counted after 30 min of nocodazole treatment and 3 min washout in karyoplasts (kpl) in different phases of Golgi biogenesis (lower panel). The number of Golgi-associated microtubules was then normalized to the total area of the Golgi precursors in the cell and the number of non-associated microtubules was normalized to the area of the remaining cytoplasm. The mean values (+s.e.m.) of four phase 1, five phase 2 and four phase 3 karyoplasts are plotted. **P*=0.035; ****P*=0.0047; n.s., non-significant. (E) GalT–GFP-expressing karyoplasts were treated with nocodazole for 30 min, and the drug was then washed out for 3 min before fixation. The samples were then immunostained for β-tubulin and for the microtubule plus-end-tip marker EB1. Asterisks indicate the karyoplast. The indicated areas of the image are magnified in the corresponding inset. e′ represents the centrosomal area of a control cell, whereas e′′ and e′′′ represent sites of microtubule nucleation from Golgi precursors of a phase 2 karyoplast. The distal location of the EB1 staining with respect to the Golgi element can be particularly appreciated in e′′′. Scale bars: 20 μm (main image); 2 μm (inset).

(Pearson's R values between 0.77 and 0.90, comparable to those of control cells in the same image; supplementary material Fig. S4B). We did not observe Sec16-positive puncta that were negative for Sec31 during phase 1 (supplementary material Fig. S4A), suggesting that the bimodal kinetics observed for the formation of Sec31-positive structures are followed by Sec16 as well.

Microtubule network reorganization during Golgi *de novo* biogenesis

Next, we investigated the role of the microtubule network in the different phases of Golgi biogenesis. After laser nanosurgery, the microtubule network showed a lack of central organization, which, by contrast, could be observed in control cells or in phase 3 karyoplasts (Fig. 6A). This result could most likely be explained by the depletion of the centrosome and, thus, the lack of centrosomal microtubule nucleation in karyoplasts. To test this hypothesis, cells were treated with 10 μM nocodazole for 30 min to depolymerize all dynamic microtubules. After this period only a few 'stable' microtubules remained in control cells and karyoplasts (data not shown). Interestingly, nocodazole washout, which is followed by the centrosomal nucleation of microtubules in control cells shortly after the washout (Fig. 6B,C), showed that even at 10 min after drug removal phase 1 cells did not nucleate microtubules (Fig. 6B). Consistent with these observations, immunostaining of EB1, a protein that is associated with the plus-end tips of growing microtubules (Galjart, 2010), was strongly reduced in phase 1 cells (Fig. 7A). The observation that a microtubule network exists at steady state in phase 1 karyoplasts (Fig. 6A) appears to be contradictory to our findings that microtubule growth is reduced in these cells (Fig. 6B,C; Fig. 7A). One explanation might be that during phase 1 microtubules are stabilized. In support of this hypothesis, microtubules in phase 1 cells showed an increased level of acetylation (Fig. 7B,C), which is a typical characteristic of stable microtubules (Westermann and Weber, 2003), compared with that observed in phase 3 and control cells (Fig. 7B,C). Nocodazole washout in phase 2 and phase 3 cells was followed by microtubule regrowth within 10 min after drug removal, although this was less efficient compared with regrowth in control cells (Fig. 6B). A central microtubule organization from the area of the newly synthesized juxta-nuclear Golgi could be observed in phase 3 cells (Fig. 6B). These observations suggest that Golgi precursors have the capacity to nucleate microtubules during phase 2 and 3. In agreement with this idea, analysis of cells at 3 min after nocodazole washout showed that phase 2 Golgi precursors were frequently associated with short microtubules (Fig. 6C). Microtubule distribution appeared to be significantly biased towards the association with Golgi elements (Fig. 6D). The association of microtubules with Golgi structures was even more pronounced in phase 3, although, at this stage, it was not yet comparable to the efficiency of microtubule nucleation of the centrosome in control cells (Fig. 6C). EB1 staining of karyoplasts in phases 2 and 3 after nocodazole washout further confirmed that the microtubules associated with Golgi precursors had been nucleated at these sites (Fig. 6E).

Golgi biogenesis is accelerated in nocodazole-treated cells

The data presented thus far are consistent with a model of Golgi *de novo* biogenesis that is based on positive-feedback loops involving microtubule network organization and ERES biogenesis that lead to the self-assembly of post-ER material and finally to the formation of a juxta-nuclear Golgi complex (Fig. 8A). On one hand, the inhibition of ER export during phase 1 could be attributed to the observed reduction in the number of ERES (Fig. 5). On the other hand, we propose that the disorganization of the microtubule network in phase 1 cells has a negative effect on the probability of small post-ER carrier fusion, which is a requirement for the formation of Golgi precursors. Indeed, under these conditions, the formation of Golgi precursors would only occur by stochastic fusion of small post-ER carriers. Nucleation of microtubules from Golgi precursors would facilitate the recruitment of small post-ER carriers and thus drastically enhance precursor growth. In turn, this growth could have a stimulatory effect on ERES biogenesis, which would additionally contribute to the observed burst of accumulation of post-ER material during phase 2.

In this model, a crucial step appears to be the fusion of small post-ER carriers, which is inhibited by the lack of organization of the microtubule network and can be drastically accelerated by the nucleation of microtubules by Golgi precursors. Therefore, the model would predict that experimental conditions that enhance the chance of small post-ER carrier fusion should accelerate Golgi *de novo* biogenesis, as well as ERES biogenesis. To test this hypothesis, we took advantage of the fact that, in nocodazole-treated cells, small post-ER carrier movement is impaired and the carriers are not efficiently moved away from their site of

Journal of Cell Science (2014) 127, 4620–4633 doi:10.1242/jcs.150474

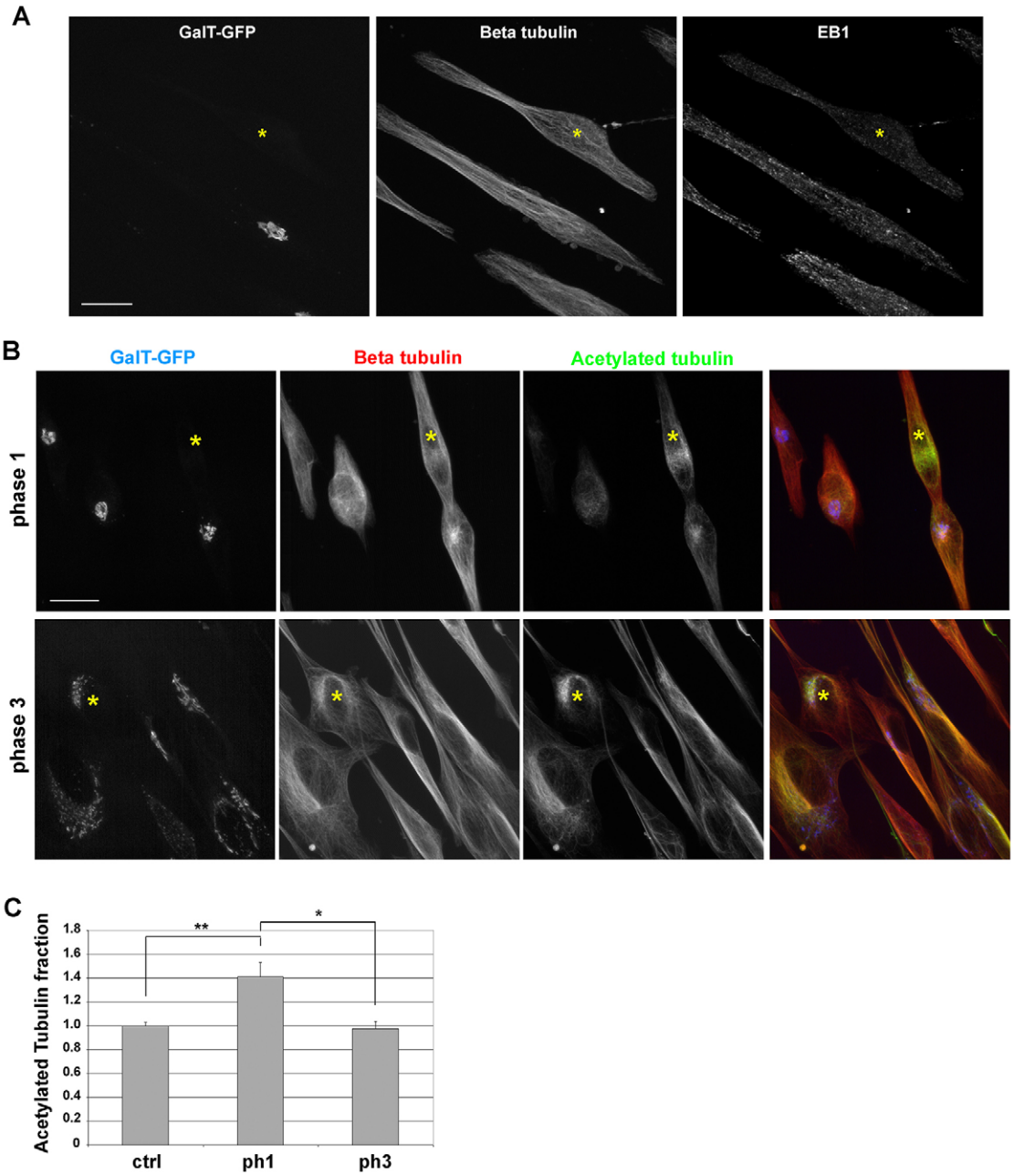

Fig. 7. Microtubules are stabilized during phase 1. A karyoplast in phase 1 was fixed and immunostained for β-tubulin and for EB1, a marker of the plus-end tips of growing microtubules. Confocal *Z*-stacks covering the entire cell thickness were acquired and the sum projection is shown. The asterisks indicate the karyoplast, which shows a strong reduction in EB1 staining compared with the neighboring unperturbed cells. Scale bar: 20 μm. (B) Karyoplasts in phase 1 or 3 were methanol fixed at −20°C for 4 min and immunostained for β-tubulin and acetylated tubulin. Confocal *Z*-stacks covering the entire cell were acquired and the sum projection is shown. Asterisks indicate the karyoplasts. Scale bar: 20 μm. (C) Cells were treated, stained and imaged as described for B. For each cell, the integrated fluorescence intensity of acetylated tubulin and β-tubulin was measured and their ratio was calculated. The ratio of karyoplasts was then divided by the value of control (ctrl) cells in the same image to determine the change in the microtubule acetylation status in the different phases of Golgi biogenesis compared with that of unperturbed cells. Data show the median+s.e.m.; $*P=0.022$; $**P=0.010$.

production (Presley et al., 1997; Scales et al., 1997), therefore enhancing the possibility that the small post-ER carriers will fuse with one another. Time-lapse analysis of nocodazole-treated karyoplasts showed that accumulation of post-ER membrane structures occurred much earlier compared with that of non-treated karyoplasts (Fig. 8B). In contrast to non-treated karyoplasts (Fig. 2A), the total fluorescence of post-ER structures increased with similar kinetics to those of the total cell fluorescence of the marker, and an inhibition of post-ER carrier formation was not observed (Fig. 8C; Fig. 2C,D). In addition, accumulation of the Golgi marker YT2 in the ER was not observed after nocodazole addition (Fig. 2E). Moreover, the amount of Sec31 associated with ERES appeared to increase earlier after laser nanosurgery in nocodazole-treated cells compared with non-treated karyoplasts (Fig. 8D). Electron microscopy analysis of nocodazole-treated karyoplasts showed

Journal of Cell Science (2014) 127, 4620–4633 doi:10.1242/jcs.150474

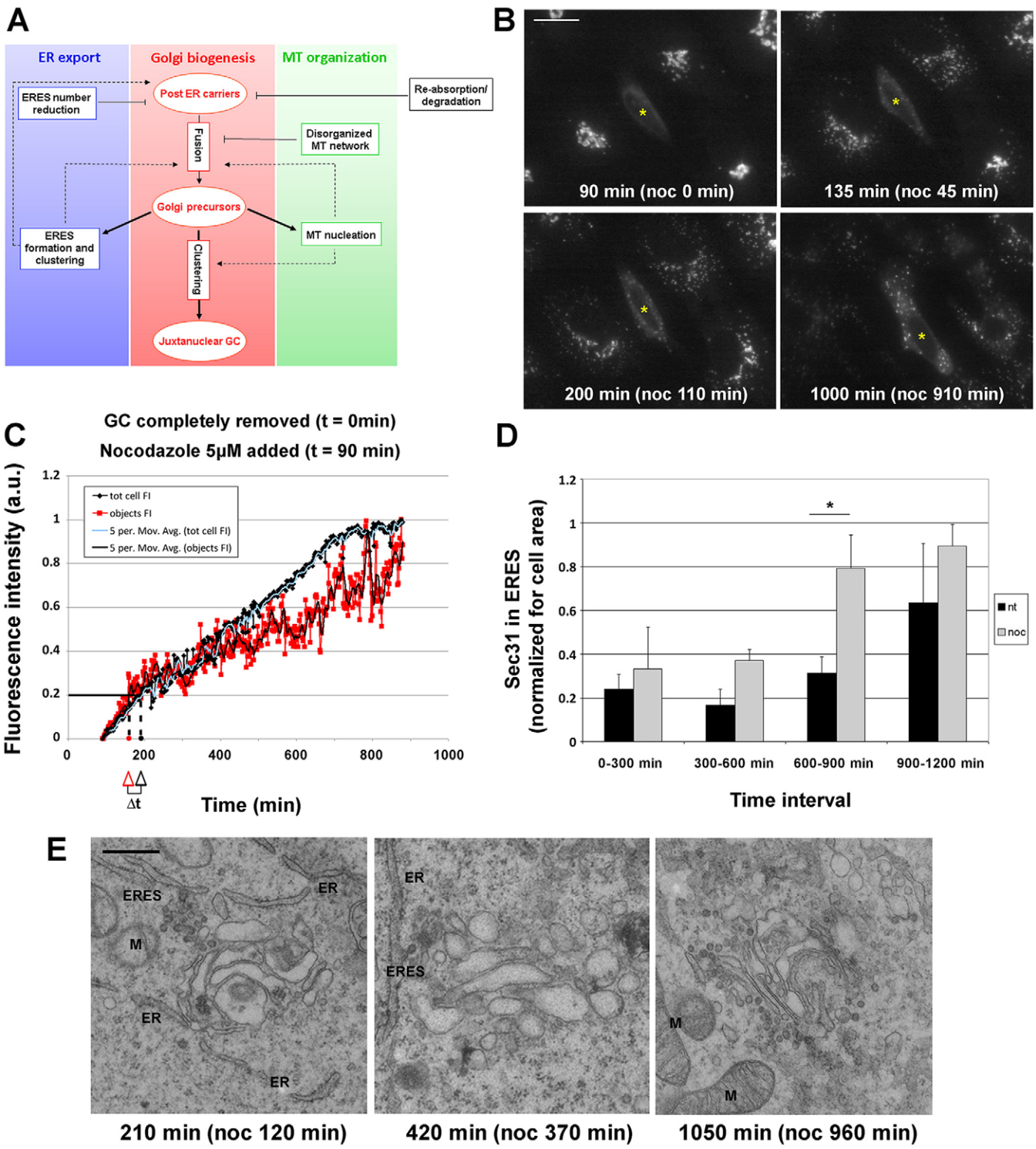

Fig. 8. See next page for legend.

that the post-ER membrane structures forming early after laser nanosurgery had Golgi-like features. Membranes appeared to be stacked and started to elongate into cisternae, although proper ministacks with flattened cisternae could be identified only at later time-points (Fig. 8E). These data demonstrate that if enough post-ER material is accumulated in a small enough area, it is able to efficiently self-organize, induce ERES biogenesis and acquire Golgi-like features.

DISCUSSION

Here, we have characterized in detail the organization and dynamics of the early secretory pathway during Golgi *de novo* biogenesis, by using our recently developed laser nanosurgery approach to deplete cells of their Golgi complex (Tängemo et al., 2011). In summary, quantitative time-lapse microscopy in combination with electron microscopy analyses revealed three phases of Golgi *de novo* biogenesis after laser nanosurgery. Phase

Journal of Cell Science

Fig. 8. Golgi biogenesis in nocodazole-treated karyoplasts is accelerated. (A) A proposed model of *de novo* biogenesis of the Golgi complex (GC), presented as a flow diagram. Elliptical shapes represent the different classes of Golgi precursors that are formed during Golgi biogenesis. Rectangular shapes represent the processes that influence their formation. Black solid lines connect the processes that influence the system during phase 1. The fusion of post-ER carriers to form Golgi precursors triggers the processes depicted with gray solid lines, which characterize phase 2 cells. The secondary effects of these processes are represented by the black dashed lines and influence Golgi biogenesis at different steps with positive-feedback loops. MT, microtubule. (B) Time-lapse imaging of a nocodazole (noc)-treated karyoplast. A YT2 cell was dissected by laser nanosurgery and 5 μM nocodazole was added to the medium at 90 min thereafter. The karyoplast was then followed by time-lapse imaging with 2-min time resolution. Still images from the movie are shown. The asterisks indicate the karyoplast. Before nocodazole addition, the karyoplasts showed the typical phase 1 net ER export block. At 45 min after nocodazole addition, post-ER accumulations of YT2 could be clearly observed and they became brighter over time. Scale bar: 20 μm. (C) Images from A were analyzed as described for Fig. 2A. The increase in fluorescence intensity (FI) in post-ER objects follows kinetics similar to those of total cell fluorescence intensity. a.u., arbitrary units. (D) Quantification of the amount of Sec31A recruited to ERES in nocodazole-treated karyoplasts during Golgi biogenesis compared with that of non-treated karyoplasts (nt). Cells were dissected by laser nanosurgery and Golgi biogenesis was followed in the presence or absence of 5 μM nocodazole. At different time-points, the cells were fixed and immunolabeled for Sec31A. Confocal *Z*-stacks covering the entire cell thickness were acquired and their sum projection was obtained. Sec31-positive ERES were segmented and their fluorescence intensity was measured in karyoplasts as well as in neighboring non-cut cells. The fluorescence intensity was then normalized to the cell area and the values of karyoplasts were divided by the average of control cells in the same image. The median (+s.e.m.) of the normalized amount of Sec31 accumulated at ERES for each time interval is plotted for nocodazole-treated and non-treated karyoplasts. $n=3$, 11, 6 and 15 non-treated and 11, 6, 5 and 5 nocodazole-treated karyoplasts for each time interval. $^*P=0.043$. (E) YT2 cells treated as described for B were fixed at the indicated time-points after nocodazole addition and processed for electron microscopy. Examples of structures identified in the karyoplasts are shown. M, mitochondria. Scale bar: 500 nm.

1 is characterized by a net inhibition of ER exit lasting for several hours before directed transport is restored and Golgi precursor growth is accelerated exponentially during phase 2. This is followed by the formation of proper Golgi ministacks that cluster in a juxta-nuclear position during phase 3.

The observed inhibition of net ER exit during phase 1 is unlikely to be the effect of laser-induced stress, as in experiments where the Golgi was only partially removed or in karyoplasts treated with nocodazole the restoration of the secretory traffic was much faster. Moreover, endocytosis of transferrin and epidermal growth factor occurred with the same efficiency as observed in unperturbed control cells under our experimental conditions. At least two observations could account for the net inhibition of ER exit in phase 1. First, the number of ERES was drastically reduced, most likely due to their depletion during laser nanosurgery. Second, small post-ER carriers occasionally formed in phase 1 and did not fuse with one another, disappearing on average 16 min after their formation as a result of their degradation or ER reabsorption.

In phase 2, which is typically much shorter than phase 1, small post-ER carriers occasionally meet and fuse with one another to form larger post-ER structures, an event that coincides with the exponential increase in the formation of further stable post-ER structures and Golgi precursors. Several of our observations indicate what factors might contribute to this exponential increase in post-ER structures. First, in contrast to smaller post-ER carriers forming in phase 1, the larger phase 2 structures are able to nucleate microtubules, as demonstrated in nocodazole washout experiments. The microtubules associated with phase 2 post-ER structures most likely provide the tracks for the small post-ER carriers to move towards and be efficiently absorbed by the larger structures, which can consequently further grow in size. The presence during phase 1 of very low levels of proteins with microtubule nucleation capability, such as AKAP450 (Rivero et al., 2009) or CLASP2 (Efimov et al., 2007), could explain the inefficiency of phase 1 structures to nucleate microtubules. Interestingly, during phase 2, the levels of Golgi-associated AKAP450 and CLASP2 are consistent with a prominent function of the latter in microtubule nucleation in this context.

Another process that could contribute to the exponential growth of post-ER material is the formation of new ERES, which increase in number about threefold during phase 2 and thus can significantly contribute to the formation of new small post-ER carriers. Interestingly, at the same time, ERES accumulate in the vicinity of the large post-ER structures. Therefore, the vesicles that they produce are able to fuse immediately and efficiently with the large post-ER structures and increase their material, without the need for long-distance microtubule-mediated transport. What are the mechanisms that induce ERES biogenesis in phase 2 karyoplasts? One possibility might be that secretory cargo and Golgi material accumulating in the ER during phase 1 (Fig. 2E) induce ERES formation, in agreement with previous findings that secretory cargo has a stimulatory activity on ER exit (Aridor et al., 1999; Forster et al., 2006; Simpson et al., 2006; Guo and Linstedt, 2006). However, we consider this possibility unlikely, as we could not observe any correlation between the amount of the YFP-tagged Golgi marker accumulating in the ER after laser nanosurgery and the onset of phase 2 (supplementary material Fig. S1C). Moreover, the number of ERES does not increase for the entire duration of phase 1 (Fig. 5C), although a continuous increase in the amount of YT2 in the ER was observed during this phase. The correlation of Golgi and ERES biogenesis suggests a coupling of Golgi and ERES formation by means of a positive-feedback loop (Fig. 8A), and therefore implicates a possible stimulating role of the Golgi precursors on ER exit and ERES biogenesis. Consistent with this hypothesis, when nocodazole accelerates Golgi biogenesis, ERES biogenesis is accelerated as well (Fig. 8D). One possibility for how this Golgi–ERES coupling could be mediated might be that Golgi precursors stabilize ERES in their vicinity and vice versa. This could be achieved by the Golgi membrane signaling to neighboring ERES through the cytosol, by retrograde traffic from Golgi precursors that could locally increase the concentration of recycling proteins in the ER (Hammond and Glick, 2000) and/or by a direct Golgi–ERES tethering, which is a generally accepted model in plant cells (daSilva et al., 2004; Staehelin and Kang, 2008; Sparkes et al., 2009; Glick, 2014). Our data propose a model of Golgi biogenesis wherein the stochastic coalescence of ER-derived carriers into larger structures triggers their capability to nucleate microtubules and stimulate ERES biogenesis, processes that, in turn, fuel the formation of the Golgi.

The ultrastructural characterization of the intermediates of Golgi biogenesis showed that the final shape of the Golgi complex is acquired in phase 3 by the flattening and stacking of a pool of convoluted interconnected membranes that had

accumulated during phase 2. Molecular characterization of phase 2 Golgi precursors showed that golgins and GRASPs are present on these structures, which could provide the adhesive forces necessary for their lateral association and fusion. However, the observation that, in nocodazole-treated karyoplasts, partially stacked Golgi precursors can be observed much earlier after laser nanosurgery (as early as 3.5 h after nanosurgery) compared to those of non-treated karyoplasts (on average 14 h) suggests that the small post-ER carriers observed in phase 1 have the intrinsic capability to self-assemble into partially stacked Golgi precursors when they coalesce. These data suggest that very low amounts of these proteins are sufficient to promote membrane tethering and stacking. By contrast, the final flattening of the partially stacked Golgi precursors and morphological transformation into proper Golgi ministacks occurs with similar kinetics after nanosurgery as in non-treated control karyoplasts, suggesting the need for the synthesis of crucial factor(s) for this process to occur. Giantin and AKAP450 could be good candidates for such factors, as they become associated with the Golgi elements only in phase 3. Taken together, our data demonstrate that the processes of Golgi biogenesis, ERES biogenesis and microtubule network organization are integrated in positive-feedback loops that guarantee the efficient formation and maintenance of the structure and function of the early secretory pathway.

MATERIALS AND METHODS

Antibodies and reagents

The antibodies used were as follows: mouse anti-GM130 (BD Biosciences), rabbit anti-AKAP450 (Sigma), rabbit anti-giantin (Abcam), mouse anti-Sec31A (BD Biosciences), rabbit anti-Sec16A (Bethyl Laboratories), mouse anti-α-tubulin (Neomarkers), rabbit anti-β-tubulin (Abcam), mouse anti-acetylated-tubulin (Sigma), mouse anti-EB1 (BD Biosciences), rat anti-EB1 (Abcam) and mouse anti-EEA1 (BD Biosciences). Sheep anti-GRASP65, sheep anti-GRASP55 and rabbit anti-CLASP2 were gifts of Martin Lowe (University of Manchester, UK), Francis Barr (University of Oxford, UK) and Irina Kaverina (Vanderbilt School of Medicine, Nashville, TN), respectively. All cell culture reagents were purchased from Gibco.

Microcontact printing and laser nanosurgery

The patterning was performed as described previously (Pouthas et al., 2008; Tängemo et al., 2011) from a photolithography mask produced by GeSim (Dresden, Germany). Laser nanosurgery was performed with a pulsed 355-nm laser (DPSL-355/14, Rapp Optoelectronic, Hamburg, Germany) coupled in an Olympus CellR widefield microscope. The pulse duration of the laser source was 1 ns with a repetition rate up to 200 Hz. The laser beam was focused and moved on the sample with an integrated UGA-40 scanner (Rapp OptoElectronic). All nanosurgery experiments were performed with a 60× water-immersion objective.

Light microscopy imaging

Live imaging of karyoplasts after nanosurgery was performed with the multi-position time-lapse microscope Cell^R (Olympus). After immunofluorescence experiments, samples were imaged with LSM510 (Zeiss), SP2 or SP5 laser scanning confocal microscopes (Leica Microsystems).

Tracking of carriers

High-temporal-resolution time-lapse movies (15-s interval between acquisitions) were analyzed with ImageJ software, and the movements of carriers were tracked ('Manual tracking' plugin). The centre of the nucleus was set as the reference point. The 2D net movement of the trajectories during the time-lapses (5 min) was determined, and the component parallel to the cell axis was calculated. Movements were defined as positive when moving away from the reference point and negative when moving towards it.

Segmentation and quantification methods

Morphoquant

For automated object (post-ER structure) detection in fluorescence images of Golgi reformation we developed a Matlab-based image-processing software (Morphoquant; Gonzalez et al., 2004). The software facilitates automated detection of locally bright structures of both small dot-like or large arbitrary shape. The segmentation can be adapted by the following parameters: objects, diameter and threshold; noise suppression, minimal area of an object. For any choice of parameters, the resulting object detection can be visually inspected on an image of choice. Once optimal parameters have been identified, the software runs automatically on multiple data sets (for background subtraction and measurement of total cell fluorescence the user provides additional images with background and cell masks). For each cell and each movie frame, the software outputs the integrated optical density of all objects [object fluorescence intensity (FI)] as well as of the entire cell (total cell fluorescence intensity) (Fig. 2).

ERES and early endosome quantification

To determine the Sec31 and EEA1 clustering index (Fig. 5D and supplementary material Fig. S2D, respectively), images acquired and processed as described above were treated as follows: (1) from the YT2 channel, a mask around the Golgi structure(s) was manually drawn. In the case of phase 1 karyoplasts, where post-ER structures could not be identified, the mask was designed to cover a random area in the perinuclear area. (2) The mask was projected on the Sec31 or EEA1 channel, and the fluorescence intensity in this area was measured (FI-Golgi). (3) The mask was then rotated 180° around the nucleus and Sec31 and EEA1 fluorescence intensity was measured (FI-opposite_side). (4) The ratio FI-Golgi:FI-opposite_side (clustering index) was measured for karyoplasts and control cells.

Electron microscopy

Correlative light and electron microscopy was performed as described previously (Colombelli et al., 2008; Tängemo et al., 2011). Epon serial sections were then collected and imaged with a Philips Biotwin CM120 electron microscope. For electron tomography, thicker serial sections (250–300 nm) were cut and collected on electron microscopy grids. Colloidal gold particles were then deposited on both surfaces to allow subsequent alignment of the tilted images. The tilted series of the cells of interest were then acquired with a TECNAI F30 (FEI) and the 3D reconstruction of the tomograms was carried out using the IMOD software (Kremer et al., 1996). Regions of interest were segmented using the same software.

Acknowledgements

We thank Uta Haselmann and Charlotta Funaya (Electron Microscopy Core Facility at EMBL) for technical support. We are grateful to Martin Lowe, Francis Barr and Irina Kaverina for sharing reagents, and to all members of the Pepperkok team and the Advanced Light Microscopy Facility at EMBL for discussions and comments on the manuscript.

Competing interests

The authors declare no competing interests.

Author contributions

P.R. and R.P. conceived of the study and wrote the manuscript; P.R. conducted the experiments; C.T. developed Morphoquant software; D.A. helped with EM tomography.

Funding

This work was supported by EMBL; and the European Union Systems Microscopy Network of Excellence [grant number FP7/2007-2013-258068]. P.R. was supported by a fellowship from the Alexander von Humboldt Foundation.

Supplementary material

Supplementary material available online at
http://jcs.biologists.org/lookup/suppl/doi:10.1242/jcs.150474/-/DC1

References

Altan-Bonnet, N., Sougrat, R., Liu, W., Snapp, E. L., Ward, T. and Lippincott-Schwartz, J. (2006). Golgi inheritance in mammalian cells is mediated through endoplasmic reticulum export activities. *Mol. Biol. Cell* **17**, 990-1005.

Aridor, M., Bannykh, S. I., Rowe, T. and Balch, W. E. (1999). Cargo can modulate COPII vesicle formation from the endoplasmic reticulum. *J. Biol. Chem.* **274**, 4389-4399.

Axelsson, M. A. and Warren, G. (2004). Rapid, endoplasmic reticulum-independent diffusion of the mitotic Golgi haze. *Mol. Biol. Cell* **15**, 1843-1852.

Budnik, A. and Stephens, D. J. (2009). ER exit sites – localization and control of COPII vesicle formation. *FEBS Lett.* **583**, 3796-3803.

Colombelli, J., Tängemo, C., Haselman, U., Antony, C., Stelzer, E. H., Pepperkok, R. and Reynaud, E. G. (2008). A correlative light and electron microscopy method based on laser micropatterning and etching. *Methods Mol. Biol.* **457**, 203-213.

Connerly, P. L., Esaki, M., Montegna, E. A., Strongin, D. E., Levi, S., Soderholm, J. and Glick, B. S. (2005). Sec16 is a determinant of transitional ER organization. *Curr. Biol.* **15**, 1439-1447.

Dacks, J. B., Peden, A. A. and Field, M. C. (2009). Evolution of specificity in the eukaryotic endomembrane system. *Int. J. Biochem. Cell Biol.* **41**, 330-340.

daSilva, L. L., Snapp, E. L., Denecke, J., Lippincott-Schwartz, J., Hawes, C. and Brandizzi, F. (2004). Endoplasmic reticulum export sites and Golgi bodies behave as single mobile secretory units in plant cells. *Plant Cell* **16**, 1753-1771.

Efimov, A., Kharitonov, A., Efimova, N., Loncarek, J., Miller, P. M., Andreyeva, N., Gleeson, P., Galjart, N., Maia, A. R., McLeod, I. X. et al. (2007). Asymmetric CLASP-dependent nucleation of noncentrosomal microtubules at the trans-Golgi network. *Dev. Cell* **12**, 917-930.

Forster, R., Weiss, M., Zimmermann, T., Reynaud, E. G., Verissimo, F., Stephens, D. J. and Pepperkok, R. (2006). Secretory cargo regulates the turnover of COPII subunits at single ER exit sites. *Curr. Biol.* **16**, 173-179.

Galjart, N. (2010). Plus-end-tracking proteins and their interactions at microtubule ends. *Curr. Biol.* **20**, R528-R537.

Gerstman, B. S. and Chapagain, P. P. (2005). Self-organization in protein folding and the hydrophobic interaction. *J. Chem. Phys.* **123**, 054901.

Glick, B. S. (2000). Organization of the Golgi apparatus. *Curr. Opin. Cell Biol.* **12**, 450-456.

Glick, B. S. (2014). Integrated self-organization of transitional ER and early Golgi compartments. *BioEssays* **36**, 129-133.

Gonzalez, R. C., Woods, R. E. and Eddins, S. L. (2004) *Digital Image Processing Using Matlab*. Upper Saddle River, NJ: Pearson Prentice Hall.

Griffiths, G., Fuller, S. D., Back, R., Hollinshead, M., Pfeiffer, S. and Simons, K. (1989). The dynamic nature of the Golgi complex. *J. Cell Biol.* **108**, 277-297.

Guo, Y. and Linstedt, A. D. (2006). COPII-Golgi protein interactions regulate COPII coat assembly and Golgi size. *J. Cell Biol.* **174**, 53-63.

Hammond, A. T. and Glick, B. S. (2000). Dynamics of transitional endoplasmic reticulum sites in vertebrate cells. *Mol. Biol. Cell* **11**, 3013-3030.

Hughes, H., Budnik, A., Schmidt, K., Palmer, K. J., Mantell, J., Noakes, C., Johnson, A., Carter, D. A., Verkade, P., Watson, P. et al. (2009). Organisation of human ER-exit sites: requirements for the localisation of Sec16 to transitional ER. *J. Cell Sci.* **122**, 2924-2934.

Ivan, V., de Voer, G., Xanthakis, D., Spoorendonk, K. M., Kondylis, V. and Rabouille, C. (2008). Drosophila Sec16 mediates the biogenesis of tER sites upstream of Sar1 through an arginine-rich motif. *Mol. Biol. Cell* **19**, 4352-4365.

Jesch, S. A., Mehta, A. J., Velliste, M., Murphy, R. F. and Linstedt, A. D. (2001). Mitotic Golgi is in a dynamic equilibrium between clustered and free vesicles independent of the ER. *Traffic* **2**, 873-884.

Kano, F., Tanaka, A. R., Yamauchi, S., Kondo, H. and Murata, M. (2004). Cdc2 kinase-dependent disassembly of endoplasmic reticulum (ER) exit sites inhibits ER-to-Golgi vesicular transport during mitosis. *Mol. Biol. Cell* **15**, 4289-4298.

Kasap, M., Thomas, S., Danaher, E., Holton, V., Jiang, S. and Storrie, B. (2004). Dynamic nucleation of Golgi apparatus assembly from the endoplasmic reticulum in interphase hela cells. *Traffic* **5**, 595-605.

Keller, P., Toomre, D., Díaz, E., White, J. and Simons, K. (2001). Multicolour imaging of post-Golgi sorting and trafficking in live cells. *Nat. Cell Biol.* **3**, 140-149.

Koreishi, M., Yu, S., Oda, M., Honjo, Y. and Satoh, A. (2013). CK2 phosphorylates Sec31 and regulates ER-To-Golgi trafficking. *PLoS ONE* **8**, e54382.

Kremer, J. R., Mastronarde, D. N. and McIntosh, J. R. (1996). Computer visualization of three-dimensional image data using IMOD. *J. Struct. Biol.* **116**, 71-76.

Lippincott-Schwartz, J. and Zaal, K. J. (2000). Cell cycle maintenance and biogenesis of the Golgi complex. *Histochem. Cell Biol.* **114**, 93-103.

Lippincott-Schwartz, J., Yuan, L. C., Bonifacino, J. S. and Klausner, R. D. (1989). Rapid redistribution of Golgi proteins into the ER in cells treated with brefeldin A: evidence for membrane cycling from Golgi to ER. *Cell* **56**, 801-813.

Lowe, M. and Barr, F. A. (2007). Inheritance and biogenesis of organelles in the secretory pathway. *Nat. Rev. Mol. Cell Biol.* **8**, 429-439.

Miles, S., McManus, H., Forsten, K. E. and Storrie, B. (2001). Evidence that the entire Golgi apparatus cycles in interphase HeLa cells: sensitivity of Golgi matrix proteins to an ER exit block. *J. Cell Biol.* **155**, 543-556.

Misteli, T. (2001). The concept of self-organization in cellular architecture. *J. Cell Biol.* **155**, 181-186.

Nédélec, F. J., Surrey, T., Maggs, A. C. and Leibler, S. (1997). Self-organization of microtubules and motors. *Nature* **389**, 305-308.

Palade, G. E. (1983). Membrane biogenesis: an overview. *Methods Enzymol.* **96**, xxix-lv.

Pouthas, F., Girard, P., Lecaudey, V., Ly, T. B., Gilmour, D., Boulin, C., Pepperkok, R. and Reynaud, E. G. (2008). In migrating cells, the Golgi complex and the position of the centrosome depend on geometrical constraints of the substratum. *J. Cell Sci.* **121**, 2406-2414.

Prescott, A. R., Farmaki, T., Thomson, C., James, J., Paccaud, J. P., Tang, B. L., Hong, W., Quinn, M., Ponnambalam, S. and Lucocq, J. (2001). Evidence for prebudding arrest of ER export in animal cell mitosis and its role in generating Golgi partitioning intermediates. *Traffic* **2**, 321-335.

Presley, J. F., Cole, N. B., Schroer, T. A., Hirschberg, K., Zaal, K. J. and Lippincott-Schwartz, J. (1997). ER-to-Golgi transport visualized in living cells. *Nature* **389**, 81-85.

Puri, S. and Linstedt, A. D. (2003). Capacity of the golgi apparatus for biogenesis from the endoplasmic reticulum. *Mol. Biol. Cell* **14**, 5011-5018.

Rivero, S., Cardenas, J., Bornens, M. and Rios, R. M. (2009). Microtubule nucleation at the cis-side of the Golgi apparatus requires AKAP450 and GM130. *EMBO J.* **28**, 1016-1028.

Ronchi, P. and Pepperkok, R. (2013). Golgi depletion from living cells with laser nanosurgery. *Methods Cell Biol.* **118**, 311-324.

Ronchi, P., Terjung, S. and Pepperkok, R. (2012). At the cutting edge: applications and perspectives of laser nanosurgery in cell biology. *Biol. Chem.* **393**, 235-248.

Scales, S. J., Pepperkok, R. and Kreis, T. E. (1997). Visualization of ER-to-Golgi transport in living cells reveals a sequential mode of action for COPII and COPI. *Cell* **90**, 1137-1148.

Seemann, J., Pypaert, M., Taguchi, T., Malsam, J. and Warren, G. (2002). Partitioning of the matrix fraction of the Golgi apparatus during mitosis in animal cells. *Science* **295**, 848-851.

Shorter, J. and Warren, G. (1999). A role for the vesicle tethering protein, p115, in the post-mitotic stacking of reassembling Golgi cisternae in a cell-free system. *J. Cell Biol.* **146**, 57-70.

Shorter, J. and Warren, G. (2002). Golgi architecture and inheritance. *Annu. Rev. Cell Dev. Biol.* **18**, 379-420.

Simpson, J. C., Nilsson, T. and Pepperkok, R. (2006). Biogenesis of tubular ER-to-Golgi transport intermediates. *Mol. Biol. Cell* **17**, 723-737.

Sparkes, I. A., Ketelaar, T., de Ruijter, N. C. and Hawes, C. (2009). Grab a Golgi: laser trapping of Golgi bodies reveals in vivo interactions with the endoplasmic reticulum. *Traffic* **10**, 567-571.

Staehelin, L. A. and Kang, B. H. (2008). Nanoscale architecture of endoplasmic reticulum export sites and of Golgi membranes as determined by electron tomography. *Plant Physiol.* **147**, 1454-1468.

Storrie, B., White, J., Röttger, S., Stelzer, E. H., Suganuma, T. and Nilsson, T. (1998). Recycling of golgi-resident glycosyltransferases through the ER reveals a novel pathway and provides an explanation for nocodazole-induced Golgi scattering. *J. Cell Biol.* **143**, 1505-1521.

Tängemo, C., Ronchi, P., Colombelli, J., Haselmann, U., Simpson, J. C., Antony, C., Stelzer, E. H., Pepperkok, R. and Reynaud, E. G. (2011). A novel laser nanosurgery approach supports *de novo* Golgi biogenesis in mammalian cells. *J. Cell Sci.* **124**, 978-987.

Trucco, A., Polishchuk, R. S., Martella, O., Di Pentima, A., Fusella, A., Di Giandomenico, D., San Pietro, E., Beznoussenko, G. V., Polishchuk, E. V., Baldassarre, M. et al. (2004). Secretory traffic triggers the formation of tubular continuities across Golgi sub-compartments. *Nat. Cell Biol.* **6**, 1071-1081.

Vignaud, T., Blanchoin, L. and Théry, M. (2012). Directed cytoskeleton self-organization. *Trends Cell Biol.* **22**, 671-682.

Wang, Y. and Seemann, J. (2011). Golgi biogenesis. *Cold Spring Harb. Perspect. Biol.* **3**, a005330.

Ward, T. H., Polishchuk, R. S., Caplan, S., Hirschberg, K. and Lippincott-Schwartz, J. (2001). Maintenance of Golgi structure and function depends on the integrity of ER export. *J. Cell Biol.* **155**, 557-570.

Warren, G. and Wickner, W. (1996). Organelle inheritance. *Cell* **84**, 395-400.

Wei, J. H. and Seemann, J. (2009). Mitotic division of the mammalian Golgi apparatus. *Semin. Cell Dev. Biol.* **20**, 810-816.

Wei, J. H. and Seemann, J. (2010). Unraveling the Golgi ribbon. *Traffic* **11**, 1391-1400.

Wennekamp, S., Mesecke, S., Nédélec, F. and Hiiragi, T. (2013). A self-organization framework for symmetry breaking in the mammalian embryo. *Nat. Rev. Mol. Cell Biol.* **14**, 452-459.

Westermann, S. and Weber, K. (2003). Post-translational modifications regulate microtubule function. *Nat. Rev. Mol. Cell Biol.* **4**, 938-948.

Zaal, K. J., Smith, C. L., Polishchuk, R. S., Altan, N., Cole, N. B., Ellenberg, J., Hirschberg, K., Presley, J. F., Roberts, T. H., Siggia, E. et al. (1999). Golgi membranes are absorbed into and reemerge from the ER during mitosis. *Cell* **99**, 589-601.

Supplementary figure legends

Figure S1. Characterization of Golgi de novo biogenesis after laser nanosurgery

A) Additional examples of analyses of the time-lapse imaging of Golgi de novo biogenesis. Karyoplasts were generated by laser nanosurgery and time-lapse imaging was performed and analyzed as in 2A with different time resolution (2-5-60minutes). The plots monitor the changes of the total cellular fluorescence intensity (F.I.) of the Golgi marker YT2 (black line) and the F.I. in segmented structures (red line) over time and show the bimodal kinetics of Golgi de novo biogenesis.

B) ER export inhibition during phase 1 is not specific for YT2. YT2 cells growing on patterned coverslips for 48h were infected with an adenoviral vector for the expression of GPI-CFP. After 1h incubation, cells were washed and left for 3h before nanosurgery. The karyoplast (asterisk) was then followed by 2 color time lapse imaging to monitor the behavior of the Golgi marker YT2 and of the other cargo GPI-CFP. Both proteins are accumulated in the ER during phase 1, and they appear in the same carriers at later time points and during phase 2. No GPI-CFP is found at the plasma membrane, in contrast with neighboring control cells. Arrowheads point at small carriers, arrows at larger intermediates positive for both YT2 and GPI-CFP. Scale bar, 20 μm.

C) The burst of ER export does not depend on the amount of protein synthesized. Golgi biogenesis after complete organelle removal in 9 karyoplast was analyzed with Morphoquant. We derived the total cell F.I. at the time of the start of the ER export burst and considered as max F.I. the plateau level of the total F.I. curve. The chart represents the percentage of the total F.I. at the time when the object F.I. reaches 20% of the max.

D) The GC in phase 3 does not show a preferential position. Radar plot of the location of the GC in phase 3 with respect to its position before laser nanosurgery. 22 karyoplasts were followed by time lapse microscopy and the position of the GC in phase 3 was determined. Positions were then classified into 4 classes (0˚, same side of old GC => positions from -45˚ to +45˚; +90˚=> from

+45˚ to +135˚; -90˚=> -45˚ to -135˚; 180˚, opposite side of the old GC => from +135˚ to -135˚). Values on the axes represent the number of cells with the GC in the corresponding position. The distribution frequency reflects the elongated cell shape and does not show a preferential site for new GC clustering.

Figure S2. Endocytosis during Golgi biogenesis

A) 1-2h after Golgi depletion cells were incubated for 1h in serum-free medium, followed by treatment with Alexa568-labelled transferrin or EGF 2μg/ml for 15 min. Cells were then extensively washed with PBS to remove the non internalized fraction and fixed with PFA. Under this experimental condition, no extracellular EGF or transferrin could be detected (not shown). Confocal z-stacks of images covering the entire cell thickness were acquired and the sum intensity projection is shown for transferrin and EGF. Asterisks indicate the karyoplasts. Scale bars, 20μm.

B) Images obtained as described in A were quantified. After background subtraction, cell outlines were manually segmented and the total F.I. in the cells was quantified and normalized for cell area. In all cases, karyoplasts' values were then divided by the average of control cells in the same image and values for single phase 1 karyoplasts are shown in the plot.

C) Karyoplasts were fixed in phase 1 or 3 and immunostained for the early endosome marker EEA1. Confocal images covering the entire cell thickness were acquired and the projection is shown. Asterisks indicate the karyoplasts. Scale bars, 20 μm.

D) EEA1 clustering index was performed as described in fig.4D and in material and methods. 26, 10 and 7 cells were analyzed for control conditions, karyoplasts ph1 and ph3, respectively. Error bars = s.e.m.

Figure S3. CLEM of YT2 positive structures

A) Time-lapse imaging of Golgi *de novo* biogenesis. After laser nanosurgery, cells were followed by time lapse microscopy until they reached the phase of interest (phase 3 in this case). For an easier visualization, a binucleated karyoplast was chosen. Asterisk = karyoplast; square, round and triangle highlight neighboring cells. These symbols indicate the same cells in B and C. Scale bar, 20 µm.

B) Before fixation higher resolution images of the karyoplast (asterisk) were acquired. The DIC image clearly shows the coverslip etching inside the glass. The outline of the karyoplast's nuclei is shown by the dashed red line for better orientation in the following correlation between light and electron microscopy images. Scale bar, 20 µm.

C) Cell were then fixed, treated with OsO_4 and before embedding the coverslip surface was etched around the karyoplast with a pattern that can be later retrieved on the surface of the resin block as previously reported (Taengemo et al., 2011). This image shows a montage of 3 images that cover the entire area between the etched patterns. The resin block is later trimmed around the groves left with laser etching and serial sections were acquired. Scale bar, 20 µm.

D) The cell of interest is identified by means of particular features of the karyoplast (e.g. the 2 nuclei in this case), the shape of the neighboring cells, as well as the presence of other characteristic features (e.g. glass fragments or cell debris in the area that can be visualized both by light and electron microscopy – arrowheads).

E) Areas of the karyoplast containing interesting YT2 positive structures are identified with the help of cellular shape features and analyzed by EM at different magnification to identify Golgi-like structures or characteristic intermediates (progressive enlargements of the boxed areas).

Scale bars, 20 µm in the LM and low magnification TEM images, 1 µm and 500 nm for the following EM images.

Figure S4. Sec16 colocalizes with sec31 in all the phases of Golgi biogenesis.

A) Karyoplasts were generated by laser nanosurgery and were followed by time-lapse microscopy. At different phases of Golgi biogenesis they were fixed and immunostained for Sec16 and Sec31. Sum projection of Z-stacks covering the entire volume of representative karyoplasts are shown. Insets show enlargements of the boxed area of the karyoplast in the main figure. Scale bars, 10μm and 4μm in the main figures and insets, respectively.

B) From the images in A the karyoplasts as well as control cells were manually segmented and the colocalization of the sec16 and sec31 labeling was analyzed by the Fiji software using Coloc2 plugin. Scatter plots represent the correlation between the intensities of the pixels in the 2 channels. Pearson's R values for each cell are represented on the plot.

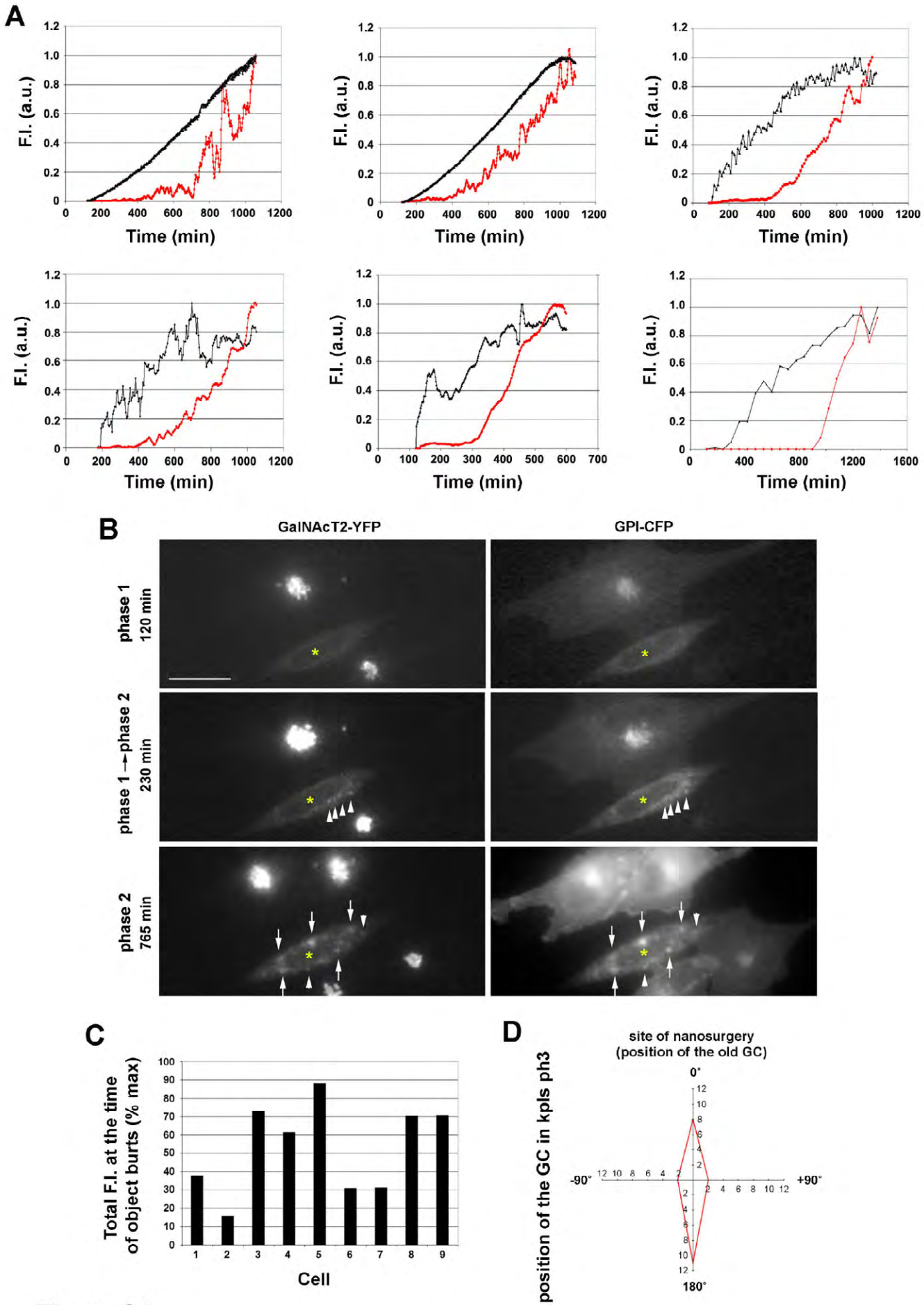
A
F.I. (a.u.)
Time (min)
B
GalNAcT2-YFP
GPI-CFP
phase 1
120 min
phase 1→phase 2
230 min
phase 2
765 min
C
Total F.I. at the time of object burts (% max)
Cell
D
site of nanosurgery
(position of the old GC)
position of the GC in kpls ph3
0°
-90°
+90°
180°

Figure S1

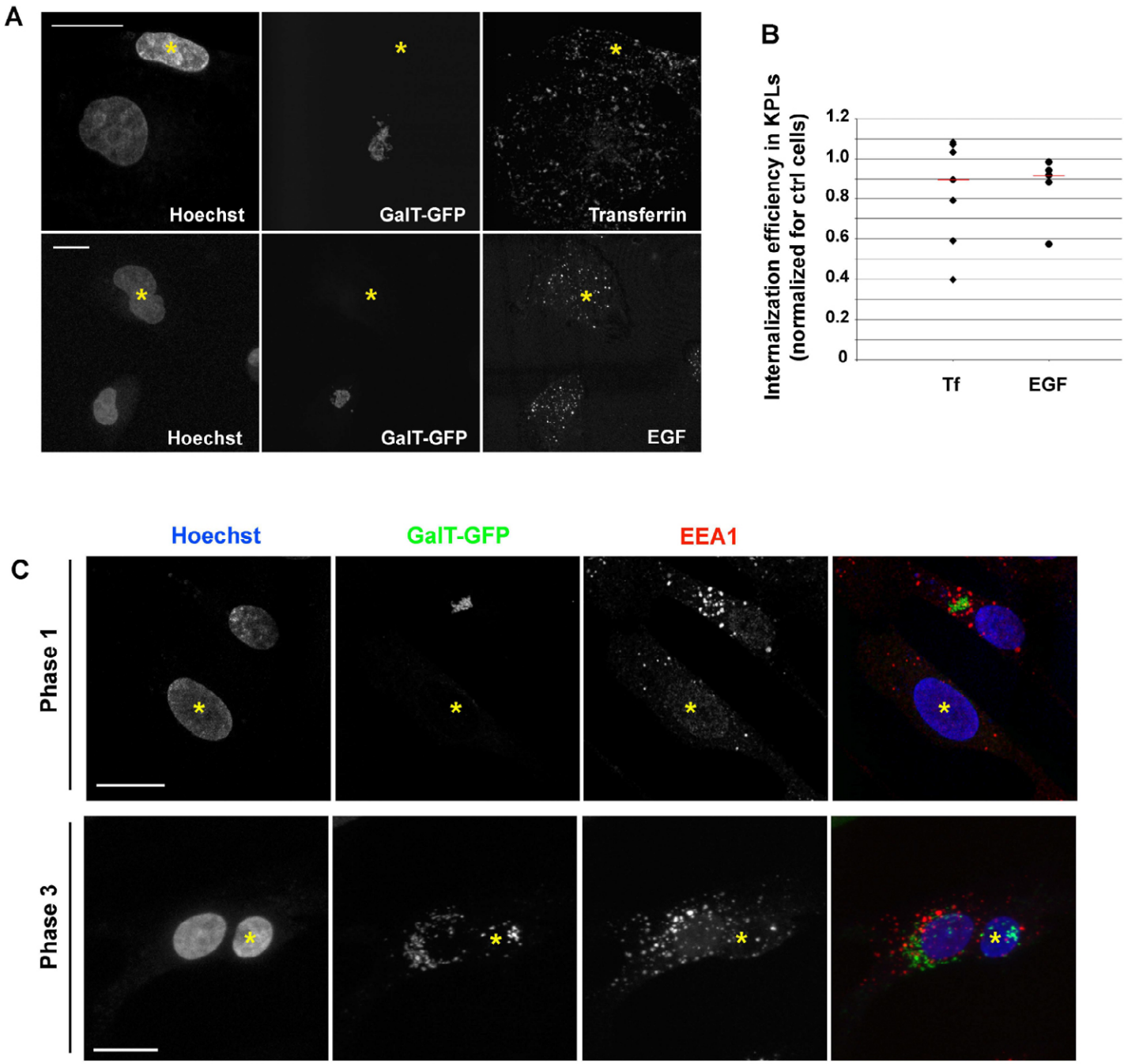
A
Hoechst
GalT-GFP
Transferrin
Hoechst
GalT-GFP
EGF
B
Internalization efficiency in KPLs (normalized for ctrl cells)
1.2
1.0
0.8
0.6
0.4
0.2
0
Tf
EGF
C
Hoechst
GalT-GFP
EEA1
Phase 1
Phase 3
D
EEA1 clustering index
25
20
15
10
5
0
Ctrl
ph1
ph3

Figure S2

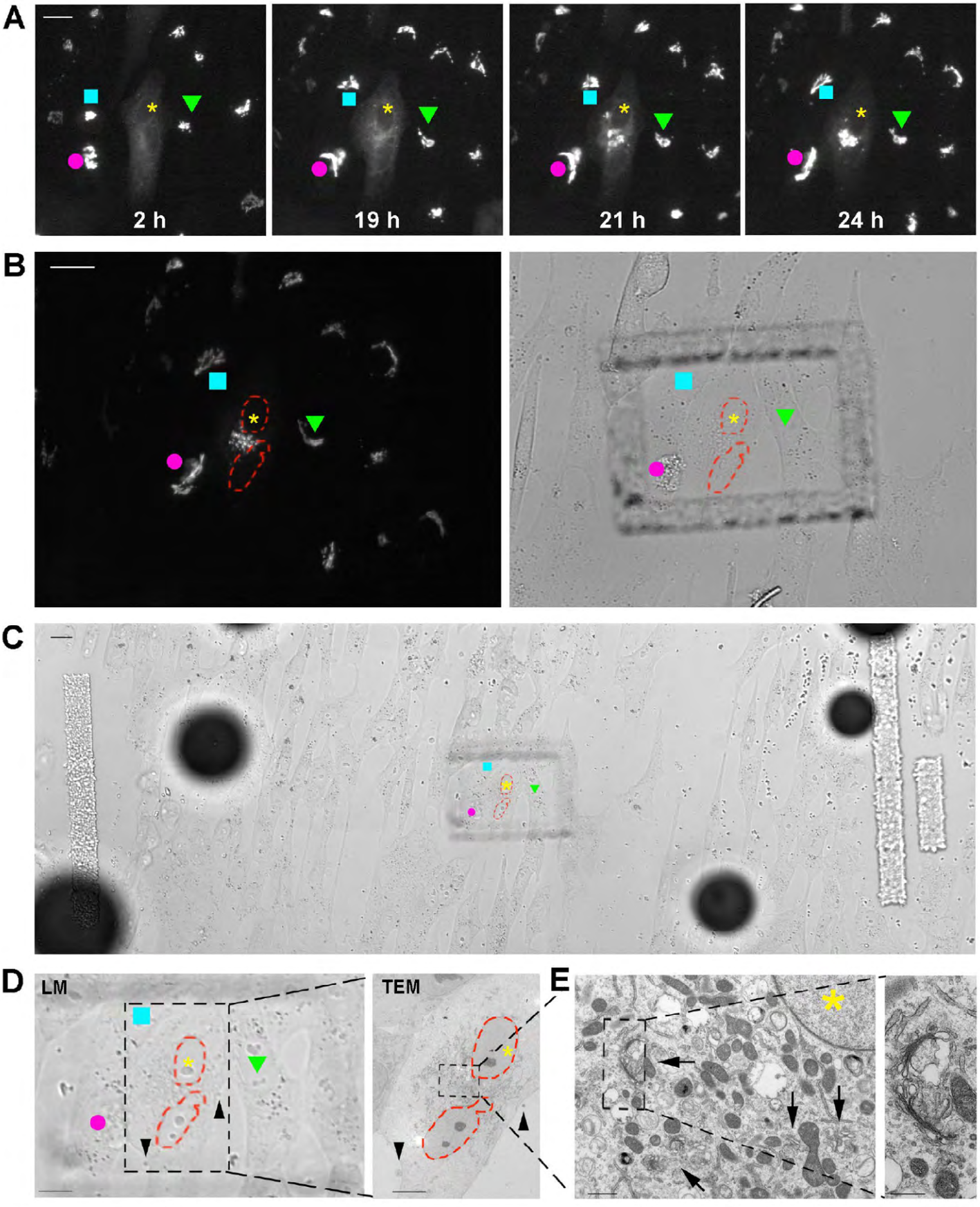

Figure S3

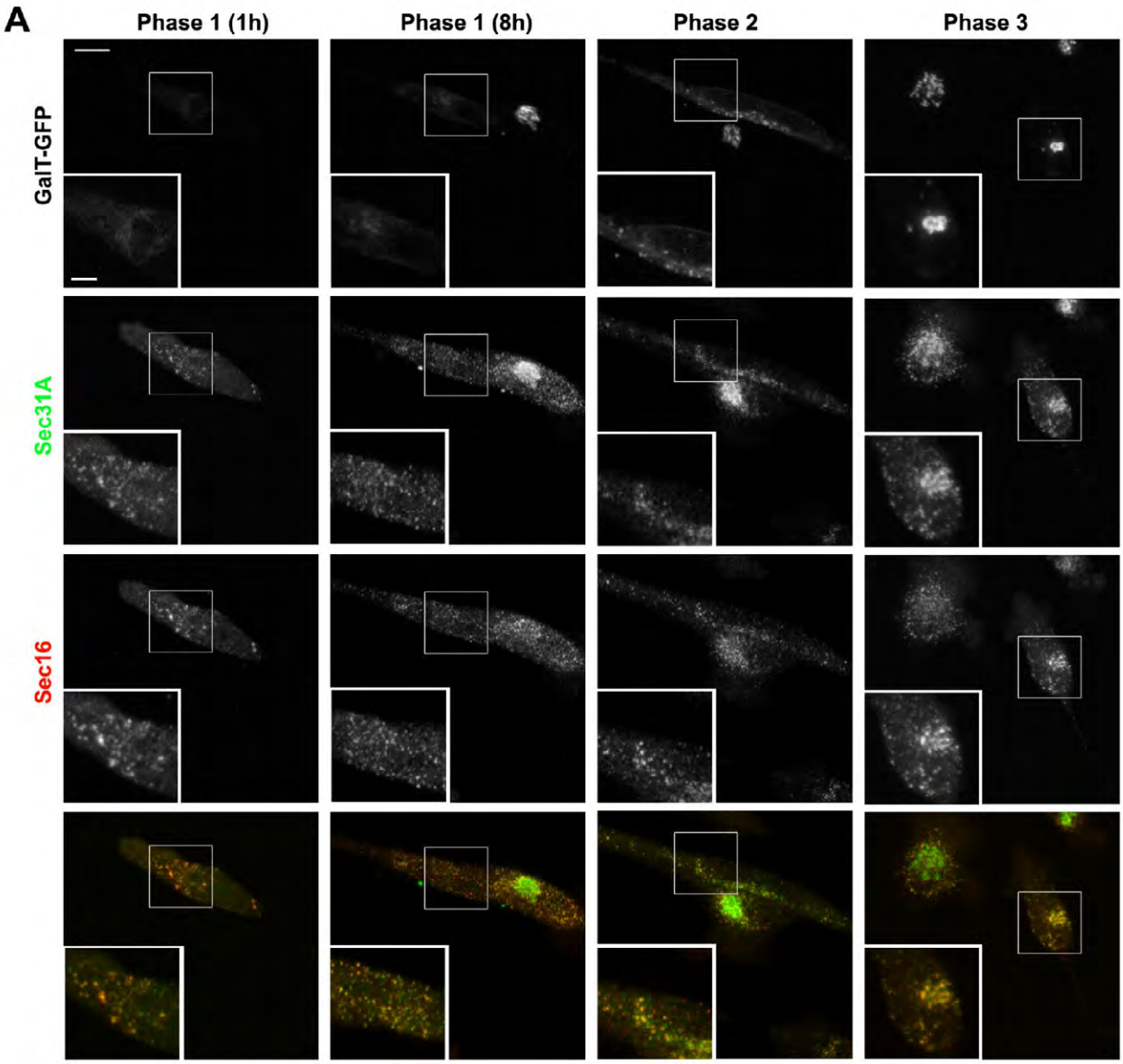
A
Phase 1 (1h)
Phase 1 (8h)
Phase 2
Phase 3
GalT-GFP
Sec31A
Sec16

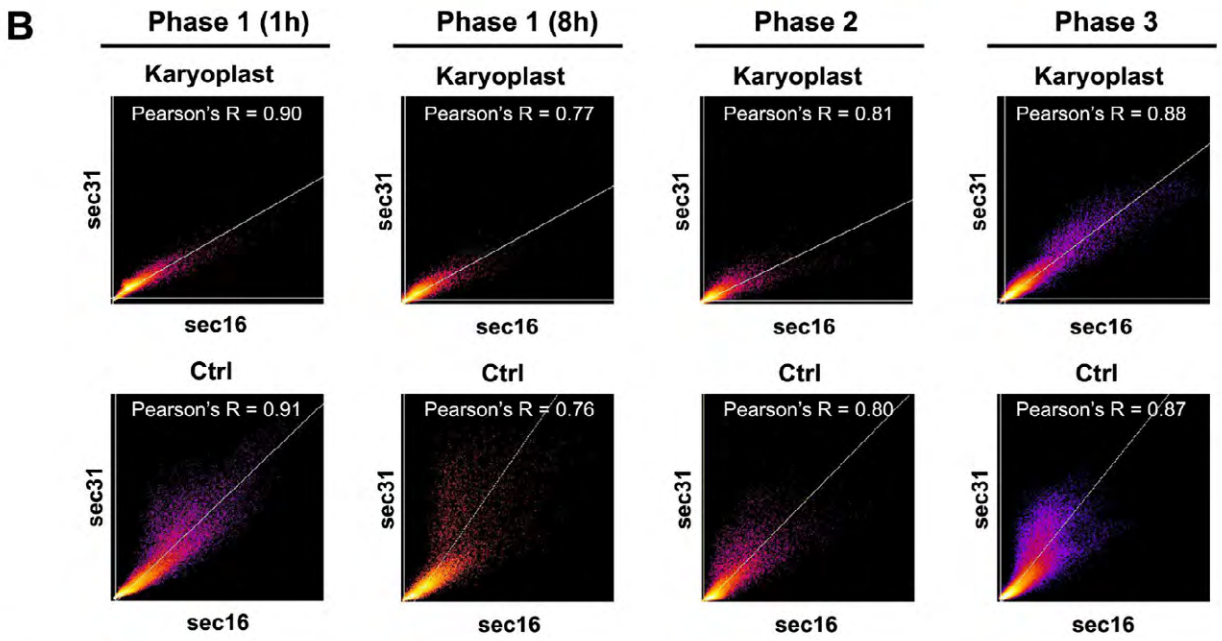
B
Phase 1 (1h)
Phase 1 (8h)
Phase 2
Phase 3
Karyoplast
Pearson's R = 0.90
Pearson's R = 0.77
Pearson's R = 0.81
Pearson's R = 0.88
Ctrl
Pearson's R = 0.91
Pearson's R = 0.76
Pearson's R = 0.80
Pearson's R = 0.87
sec31
sec16

Figure S4

Movie S1. Golgi biogenesis after laser nanosurgery in YT2 cells.

A YT2 cell was dissected by laser nanosurgery in order to completely remove the GC. Golgi biogenesis was subsequently followed by time lapse imaging (2min time resolution). The movie is reproduced with 12min resolution.

Movie S2. Electron tomography of a phase 2 structure

A YT2 cell was dissected by laser nanosurgery and followed by time lapse microscopy until it reached phase 2. The cells were then fixed and embedded for EM. Semi-thin serial sections (300nm) were obtained and tomograms of 3 consecutive sections were acquired with a FEI TECNAI F30 microscope. 3D reconstruction of the tomograms was carried out with the IMOD software. The movie shows the Z-stack of tomographic slices and the 3D reconstruction of a Golgi precursor structure. Each color represents a continuous membrane-bounded structure.